Double unstable avoided crossings and complex-domain-pattern formation in spin-orbit-coupled spin-1 condensates

Sanu Kumar Gangwar [1], Rajamanickam Ravisankar [2,3,*], Henrique Fabrelli [4]
Paulsamy Muruganandam [5,6] and Pankaj Kumar Mishra [1,†]

[1]*Department of Physics, Indian Institute of Technology, Guwahati 781039, Assam, India*
[2]*Department of Physics, Zhejiang Normal University, Jinhua, Zhejiang 321004, People's Republic of China*
[3]*Zhejiang Institute of Photoelectronics and Zhejiang Institute for Advanced Light Source, Zhejiang Normal University, Jinhua, Zhejiang 321004, China*
[4]*Centro Brasileiro de Pesquisas Físicas, 22290-180 Rio de Janeiro, Rio de Janeiro, Brazil*
[5]*Department of Physics, Bharathidasan University, Tiruchirappalli 620024, Tamil Nadu, India*
[6]*Department of Medical Physics, Bharathidasan University, Tiruchirappalli 620024, Tamil Nadu, India*

We analyze the impact of spin-orbit and Rabi couplings on the dynamical stability of spin-orbit-coupled spin-1 Bose-Einstein condensates for ferromagnetic (FM) and antiferromagnetic (AFM) interactions. Determining the collective excitation spectrum through Bogoliubov–de Gennes theory, we characterize the dynamical stability regime via modulational instability. For AFM interactions, the eigenspectrum reveals the presence of both stable and unstable avoided crossings (UACs), with the first-excited branch undergoing a double unstable avoided crossing. In contrast, with ferromagnetic interactions, only a single UAC, which occurs between the low-lying and first-excited branches, is observed. Furthermore, the eigenvectors demonstrate the transition from densitylike to spinlike behavior, as the collective excitation shows the transition from the stable to the unstable mode for both the FM and AFM interactions. In the multiband instability state, eigenvectors display spin-density mixed mode, while they show spin-flip nature in the avoided crossing regime. Our analysis suggests that spin-orbit coupling enhances the instability gain, while Rabi coupling plays the opposite role. Finally, we corroborate our analytical findings of stable and unstable regimes through numerical simulations of the dynamical evolution of the condensates by introducing the perturbations upon quenching the trap strength. The dynamical phases show the formation of complex domains with AFM interaction, which may be attributed to the double unstable avoided crossings in such a system.

I. INTRODUCTION

The experimental realization of spin-orbit-coupled (SOC) Bose-Einstein condensates (BECs) in the laboratory has opened up a wide range of phenomena to explore in ultracold atomic physics. Initially achieved in experiments using two of the three hyperfine components of the $F = 1$ states of ^{87}Rb [1] and later extended to spin-1 BECs [2,3], these systems have become a rich ground for exploring exotic quantum phenomena such as superfluidity [4], supersolidity [5], metastable supersolid [6], modulation instability [7–9], vortices [10,11], and solitons [12,13].

Numerical simulations have played a crucial role in revealing many fascinating properties of spin-orbit-coupled (SOC) Bose-Einstein condensates (BECs), primarily through the use of the mean-field Gross-Pitaevskii equation (GPE) [14–20]. Liu *et al.* reported exact soliton solutions and manifold mixing dynamics in quasi-one-dimensional SOC spin-1 BECs [21]. Numerical studies along similar lines suggest the emergence of more complex phases, such as multiring structures, stripes, and superlattice solitons, in quasi-two-dimensional

SOC spin-1 BECs [22]. In addition to these phases, the formation of symbiotic spinor solitons has been reported in quasi-one-dimensional and quasi-two-dimensional spin-1 ferromagnetic (FM) BECs [23]. For antiferromagnetic (AFM) SOC spin-1 BECs, the formation of stable multipeak vector solitons in quasi-one-dimensional systems has been reported [24]. Recently, He and Lin, through linear stability analysis, demonstrated the existence of stationary and moving bright solitons in quasi-one-dimensional SOC spin-1 BECs under the influence of a Zeeman field [25]. Several works have reported the coexistence of spin precession and the separation between the spin components because of anomalous spin-dependent velocities arising solely due to the spin-orbit coupling, which also results in the appearance of complex dynamics in the condensate [26–28].

Collective excitations, which are low-lying excitations of the quantum gas, are key in determining the stability properties of ground-state phases and the behavior of fluctuations and superfluidity of the BECs. Landau developed a framework for studying elementary excitations in superfluid helium, while for weakly interacting Bose gases, Bogoliubov derived the theory of elementary excitations [29]. Numerous theoretical works have reported the collective excitations in single-component BECs [30–33]. Goldstein and Meystre [34]

*Contact author: ravicpc2012@gmail.com

†Contact author: pankaj.mishra@iitg.ac.in

extended the Hartree-Bogoliubov theory for multicomponent BECs and derived the quasiparticle frequency spectrum. They further demonstrated that interferences arising from cross coupling between condensate components resulted in a reversal of the sign of the effective two-body interaction and the onset of spatial instabilities. The stability of supercurrents in BECs with one-dimensional spin-orbit coupling has also been studied, showing that supercurrents in the plane-wave phase exhibit dynamical instability. Additionally, extensive energetic instability analysis of supercurrent states has been reported [35]. Several laboratory experiments have reported collective excitations, including phononlike excitations in a dilute gas of ^{87}Rb [36] and collective excitations of sodium atoms in a magnetic trap [37]. Khamehchi *et al.* [38] used Bragg spectroscopy to measure the collective excitations in SOC BECs, revealing the presence of phonon-maxon-roton modes, as predicted using the Bogoliubov–de Gennes (BdG) theory. In a recent study, Ravisankar *et al.* [39] investigated the influence of spin-orbit coupling and Rabi coupling strengths on the dynamical instability of quasi-two-dimensional binary BECs using Bogoliubov theory. Their analysis revealed the presence of phonon, roton, and maxon modes, demonstrating that increasing the spin-orbit coupling enhances instability, whereas stronger Rabi coupling stabilizes the system.

Modulation instability (MI) is a measure of instability in BECs, which is one of the key criteria for determining the stability of the condensate. In recent years, numerous studies have been carried out to examine the stability of the spinor condensate using MI. For instance, Kasamatsu and Tsubota [40,41] demonstrated that MI in two-component BECs leads to the formation of multiple domains and regions dominated by solitary waves. Robins *et al.* [42] and Zhang *et al.* [43] performed numerical MI analyses of the FM and AFM phases of spin-1 BECs, revealing that the FM phase is unstable, while the AFM phase is stable. Some works show the stability analysis of these phases in the presence of the external field. For instance, Matuszewski *et al.* showed that a homogeneous magnetic field induces spatial MI in AFM spin-1 BECs, resulting in the formation of spin domains in sodium condensates confined in optical traps [44]. In a subsequent study, they found that the metastable phases of an AFM spin-1 condensate, in a simple model with pure contact interactions, could exhibit a rotonlike minimum in the excitation spectrum. The presence of an external magnetic field gives rise to the instability of the roton modes, which can lead to the spontaneous emergence of regular periodic patterns [45]. Similarly, Kronjäger *et al.* reported spontaneous pattern formation in AFM spinor BECs and identified several linearly unstable modes using a mean-field approach [46]. In another direction, Pu *et al.* reported that magnetic-field-induced dynamical instabilities in spin-1 BECs are accompanied by I_o-type instabilities in the presence of a nonzero magnetic field [47]. Systems with such embedded instabilities spontaneously develop a spatial pattern in the time evolution from the uniform initial state.

On the other hand, studies of instabilities in SOC BECs remain relatively limited. Bhuvaneswari *et al.* [8] theoretically investigated the MI in quasi-two-dimensional SOC BECs with Rabi coupling, assuming equal densities for both pseudospin components. They found that unstable modulations arise from initially miscible condensates, depending on the combination

of signs of intra- and intercomponent interaction strengths. The spin-orbit coupling enhances instability regardless of the interaction type; however, in the case of attractive interactions, spin-orbit coupling further amplifies the MI. In quasi-one-dimensional systems, Bhat *et al.* [7] demonstrated that two-component SOC BECs with equal component densities exhibit MI, leading to the formation of a striped phase as the ground state. Additionally, Li *et al.* [9] studied MI in quasi-one-dimensional SOC BECs with Raman coupling, showing that instability occurs for repulsive density-density and spin-exchange interactions even in the absence of spin-orbit coupling and Raman coupling.

Identifying unstable phases and their underlying mechanisms in complex spin-1 BECs remains a significant challenge. For instance, a recent study by Gangwar *et al.* reported the occurrence of unstable avoided crossings (UACs) in the context of FM interactions in spin-1 SOC BECs [48]. However, a comprehensive understanding of the interplay among interaction strength, spin-orbit coupling, and Rabi coupling, the key factors in the emergence of complex phases, remains elusive. In this paper, we present a detailed analysis of modulational instabilities in SOC spin-1 BECs, exploring how interaction types (AFM and FM) and coupling parameters influence the eigenspectrum and resulting dynamics. For AFM interactions, the eigenspectrum exhibits both stable and UACs between the low-lying and first-excited branches, as well as between the first-excited and second-excited branches. Notably, the first-excited branch under AFM interactions displays a double UAC, a phenomenon previously reported for spin-1 BECs in the presence of a magnetic field [46,47]. In this study, however, we explicitly demonstrate that this double unstable avoided crossing is induced by spin-orbit coupling. For FM interactions, we find that a single UAC occurs between the low-lying and first-excited branches, with a double UAC appearing only when the Rabi coupling strength is negative. The UAC is associated with the I_o-type instability, which drives pattern formation in the density profile of the condensate [49]. To complement our analytical findings, we conduct numerical simulations for both AFM and FM interactions. These simulations provide deeper insight into the dynamics and pattern formation arising from modulational instability.

The structure of our paper is as follows. In Sec. II we present the mean-field model to explore MI of SOC spin-1 BECs with Rabi coupling. Following this, we provide a detailed theoretical formalism using BdG theory to calculate the collective excitation spectrum in Sec. III. In Sec. III A we present the collective excitation spectrum for FM interactions, followed by an analysis of AFM interactions in Sec. III B. In Sec. IV we present the effect of interaction strengths on MI. In Sec. V we demonstrate the variation of the band gaps between the low-lying and first-excited states and between the first- and second-excited states for FM and AFM interaction. In Sec. VI we present numerical simulations using the GPEs, which complement the dynamical instability regions obtained from the BdG analysis. In Sec. VII we summarize our findings.

II. MEAN-FIELD MODEL

We consider a quasi-one-dimensional SOC spin-1 BECs with tight confinement in the transverse direction [50], which

can be described using three sets of coupled GPEs, given as [23,51–53]

$$i\frac{\partial \psi_{\pm 1}}{\partial t} = \left(-\frac{1}{2}\frac{\partial^2}{\partial x^2} + V(x) + c_0\rho \right)\psi_{\pm 1}$$

$$\mp \frac{k_L}{\sqrt{2}}\frac{\partial \psi_0}{\partial x} + c_2(\rho_{\pm 1} + \rho_0 - \rho_{\mp 1})\psi_{\pm 1}$$

$$+ c_2\psi_0^2\psi_{\mp 1}^* + \frac{\Omega}{\sqrt{2}}\psi_0, \tag{1a}$$

$$i\frac{\partial \psi_0}{\partial t} = \left(-\frac{1}{2}\frac{\partial^2}{\partial x^2} + V(x) + c_0\rho \right)\psi_0$$

$$+ \frac{k_L}{\sqrt{2}}\left(\frac{\partial \psi_{+1}}{\partial x} - \frac{\partial \psi_{-1}}{\partial x} \right) + c_2(\rho_{+1} + \rho_{-1})\psi_0$$

$$+ 2c_2\psi_0^*\psi_{+1}\psi_{-1} + \frac{\Omega}{\sqrt{2}}(\psi_1 + \psi_{-1}). \tag{1b}$$

Here ψ_{+1}, ψ_0, and ψ_{-1} are the spinor wave functions that satisfy the normalization condition $\int_{-\infty}^{\infty} dx\,\rho = 1$, where $\rho = \sum_{j=-1}^{1}\rho_j$, the total atomic density of the condensate, and $\rho_j = |\psi_j(x)|^2$ represents the density of jth component of the condensate with $j = \pm 1, 0$. Equations (1a) and (1b) are nondimensionalized, using time, length, and energy $t = \omega_x \tilde{t}$, $x = \tilde{x}/l_0$, and $\hbar\omega_x$, respectively. The resulting condensate wave function is $\psi_{\pm 1,0} = \sqrt{\frac{l_0}{N}}\tilde{\psi}_{\pm 1,0}$, where $l_0 = \sqrt{\hbar/m\omega_x}$ is the oscillator length for the trap frequency ω_x along the x axis. The trap strength is given by $V(x) = x^2/2$, the density-density interaction strength $c_0 = 2Nl_0(a_0 + 2a_2)/3l_\perp^2$, and the spin-exchange interaction strength $c_2 = 2Nl_0(a_2 - a_0)/3l_\perp^2$, where a_0 and a_2 are the s-wave scattering lengths in the total spin channels 0 and 2, respectively. Upon tuning $c_2 < 0$ ($c_2 > 0$), one can have the FM (AFM) interaction of the condensates [53,54]. Here $l_\perp = \sqrt{\hbar/m\omega_\perp}$ is the oscillator length in the transverse direction with $\omega_\perp = \sqrt{\omega_y\omega_z}$. The spin-orbit coupling and Rabi coupling strengths are given by $k_L = \tilde{k}_L/\omega_x l_0$ and $\Omega = \tilde{\Omega}/\hbar\omega_x$, respectively. In the above description, the quantities with the tilde represent dimensionful quantities. In this entire work, we consider all parameters to be dimensionless. The energy functional corresponding to the coupled GPEs (1a) and (1b) is given by [20]

$$E = \frac{1}{2}\int dx\left(\sum_j |\partial_x\psi_j|^2 + 2V(x)\rho + c_0\rho^2 \right.$$

$$+ c_2\big[\rho_{+1}^2 + \rho_{-1}^2 + 2\big(\rho_{+1}\rho_0 + \rho_{-1}\rho_0 - \rho_{+1}\rho_{-1}$$

$$+ \psi_{-1}^*\psi_0^2\psi_{+1}^* + \psi_{-1}\psi_0^{*2}\psi_{+1})\big] + \sqrt{2}\Omega[(\psi_{+1}^* + \psi_{-1}^*)\psi_0$$

$$+ \psi_0^*(\psi_{+1} + \psi_{-1})] + \sqrt{2}k_L[(\psi_{-1}^* - \psi_{+1}^*)\partial_x\psi_0$$

$$+ \psi_0^*(\partial_x\psi_{+1} - \partial_x\psi_{-1})]\bigg). \tag{2}$$

Here we outline the experimentally viable range for the parameters that we have considered for our simulations. For the FM interaction, we consider ^{87}Rb BECs with the number of atoms $N \sim 2 \times 10^4$. The axial trap frequency is $\omega_x = 2\pi \times 50$ Hz and the transverse trap frequencies are $\omega_y = \omega_z = 2\pi \times 500$ Hz. The resultant characteristic lengths would be $l_0 = 1.52$ μm and $l_\perp = 0.48$ μm. For the AFM interaction, we consider the BECs of ^{23}Na atoms. The resultant characteristic lengths for ^{23}Na BECs are $l_0 = 2.9$ μm and $l_\perp = 0.9$ μm. The spin-dependent and spin-independent interactions can be achieved by controlling the s-wave scattering lengths through Feshbach resonance [55–57]. However, the SOC strength $k_L = 0.1$–5 can be tuned by changing the laser wavelengths in the range from 68.86 μm to 1377.22 nm. However, the dimensionless Rabi frequency interval $\Omega = [0, 5]$ used in the simulation can be attained by tuning the Raman laser strength in the range of $2\pi\hbar \times (5$–250) Hz.

III. COLLECTIVE EXCITATION SPECTRUM

In this section, we present the collective excitation spectrum of SOC spin-1 BECs using the BdG analysis. We consider that the uniform ground-state wave function ϕ_j is perturbed by the wave function $\delta\phi_j$ for which the excited-state wave function is given by [47,58]

$$\psi_j(x, t) = e^{-i\mu_j t}[\phi_j + \delta\phi_j(x, t)], \tag{3}$$

where

$$\delta\phi_j(x, t) = u_j e^{i(q_x x - \omega t)} + v_j^* e^{-i(q_x x - \omega^* t)}, \tag{4}$$

and the uniform ground-state wave function is considered as $\phi_j = (1/2, -1/\sqrt{2}, 1/2)^T$, μ_j denotes the chemical potential, and u_j and v_j are the Bogoliubov amplitudes corresponding to the three spin components. Substituting Eq. (3) in the dynamical equations (1a) and (1b), we obtain

$$(\mathcal{L} - \omega I)(u_{+1}\ v_{+1}\ u_0\ v_0\ u_{-1}\ v_{-1})^T = 0, \tag{5}$$

where T represents the transpose of the matrix, I is a 6×6 identity matrix, and $\mathcal{L}$ is a 6×6 matrix given by

$$\mathcal{L} = \begin{pmatrix} H_+ - \mu_+ & \mathcal{L}_{12} & \mathcal{L}_{13} & \mathcal{L}_{14} & \mathcal{L}_{15} & \mathcal{L}_{16} \\ \mathcal{L}_{21} & -H_+ + \mu_+ & \mathcal{L}_{23} & \mathcal{L}_{24} & \mathcal{L}_{25} & \mathcal{L}_{26} \\ \mathcal{L}_{31} & \mathcal{L}_{32} & H_0 - \mu_0 & \mathcal{L}_{34} & \mathcal{L}_{35} & \mathcal{L}_{36} \\ \mathcal{L}_{41} & \mathcal{L}_{42} & \mathcal{L}_{43} & -H_0 + \mu_0 & \mathcal{L}_{45} & \mathcal{L}_{46} \\ \mathcal{L}_{51} & \mathcal{L}_{52} & \mathcal{L}_{53} & \mathcal{L}_{54} & H_- - \mu_- & \mathcal{L}_{56} \\ \mathcal{L}_{61} & \mathcal{L}_{62} & \mathcal{L}_{63} & \mathcal{L}_{64} & \mathcal{L}_{65} & -H_- + \mu_- \end{pmatrix}. \tag{6}$$
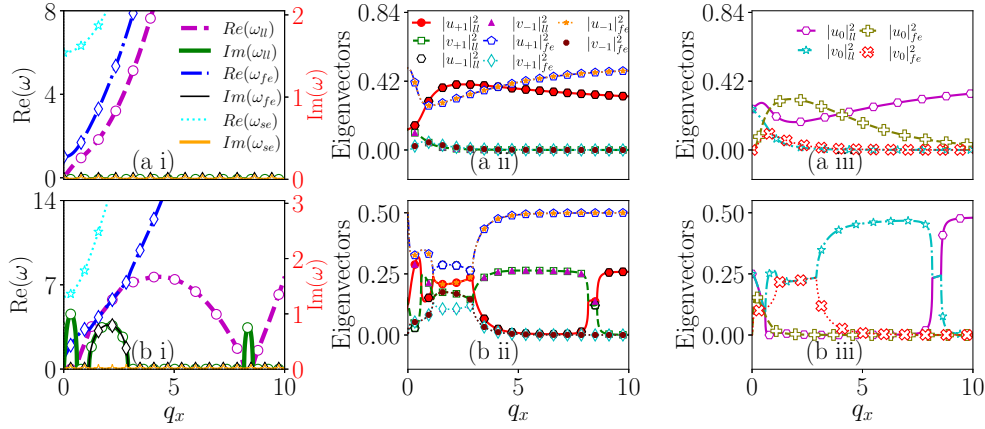
FIG. 1. Eigenvalue and corresponding eigenvectors for (a) $(k_L, \Omega) = (0.5, 1.0)$ showing real eigenfrequencies and (b) $(k_L, \Omega) = (4.5, 1.0)$ showing the multiband instability for FM interaction with $c_0 = 5$ and $c_2 = -2.0$. The magenta dashed line represents $\text{Re}(\omega_{ll})$, the thick green solid line represents $|\text{Im}(\omega_{ll})|$, the blue dash-dotted line represents $\text{Re}(\omega_{fe})$, the thin black solid line represents $|\text{Im}(\omega_{fe})|$, the cyan dotted line represents $\text{Re}(\omega_{se})$, and the thick orange solid line represents $|\text{Im}(\omega_{se})|$; here solid and dash-dotted lines are the analytical results of the BdG equation (8) and open circles are numerical results obtained by solving Eq. (5). The eigenvectors of the low-lying branch are $|u_{+1}|^2_{ll}$ (red circles), $|u_{-1}|^2_{ll}$ (black hexagons), $|u_0|^2_{ll}$ (magenta hexagons), $|v_0|^2_{ll}$ (cyan open stars), $|v_{+1}|^2_{ll}$ (green open squares), and $|v_{-1}|^2_{ll}$ (magenta triangles) and for the first-excited branch $|u_{+1}|^2_{fe}$ (blue open pentagons), $|u_{-1}|^2_{fe}$ (orange stars), $|u_0|^2_{fe}$ (olive open pluses), $|v_0|^2_{fe}$ (red open crosses with the dotted line), $|v_{+1}|^2_{fe}$ (cyan open diamonds), and $|v_{-1}|^2_{fe}$ (maroon closed circles). (a i) Only real eigenfrequencies are shown. (b i) Multiband instability, which is symmetric in the quasimomentum direction. The corresponding eigenvectors depict the densitylike mode and spinlike mode, respectively. The UAC among branches results in an I_o-type instability band in the eigenspectrum. The vertical scale on the right represents the magnitude of imaginary eigenfrequencies.

The matrix elements of $\mathcal{L}$ are provided in the Appendix. Bogoliubov coefficients follow the normalization condition

$$\int \left(\sum_j (|u_j|^2 - |v_j|^2) \right) dx = 1. \qquad (7)$$

We compute the determinant of the matrix $\mathcal{L}$ and equate it to zero $\det(\mathcal{L} - I\omega) = 0$, which yields the characteristic equation

$$\omega^6 + b\omega^4 + c\omega^2 + d = 0, \qquad (8)$$

with the coefficients b, c, and d provided in the Appendix.

By numerically solving the BdG equations (6), we complement the reliability of the analytical results for the excitation spectrum and obtain the eigenvectors as a function of q_x. For the numerical calculation, we consider the real space $[-1000, 1000]$ grid with a step size of $h_x = 0.2$. We employ the Fourier collocation method, which utilizes the LAPACK package [59] to diagonalize the truncated BdG matrix we acquire by numerically computing the Fourier transform of the BdG equations. In momentum space q_x, we consider $[-700, 700]$ modes, with a grid step size of $h_{q_x} = 0.0157$.

In our recent work, we conducted a detailed analysis of the collective excitation spectrum for FM interactions in SOC spin-1 BECs. We reported the presence of unstable avoided crossings between the low-lying and first-excited states of the eigenspectrum [48]. In this paper, we extend this analysis to AFM interactions, where we observe evidence of double avoided crossings. In the following section, first we discuss the effects of spin-orbit coupling and Rabi coupling on the eigenspectrum for FM interactions and subsequently we extend the analysis to AFM interactions.

A. Collective excitation spectrum of FM SOC BECs ($c_0 > 0$ and $c_2 < 0$)

In this section, we present the collective spectrum analysis for SOC BECs with FM interaction, characterized by $c_0 = 5.0$ and $c_2 = -2.0$. The negative (ω_-), positive (ω_+), and zeroth (ω_0) branches are designated as the low-lying (ω_{ll}), first-excited (ω_{fe}), and second-excited (ω_{se}) branches of the eigenspectrum, respectively. It has been shown that the eigenspectrum of SOC BECs exhibits intriguing features, including I_o-type instabilities [47,49]. Generally, these I_o-type instabilities arise from UACs between the branches.

We begin our analysis by first calculating the eigenvalues of the BdG matrix, as given in Eq. (6). In Fig. 1 we present the eigenspectrum corresponding to regime I ($k_L^2 < \Omega$) [Fig. 1(a)] and regime II ($k_L^2 > \Omega$) [Fig. 1(b)] of the condensate. In regime I ($k_L^2 < \Omega$), we observe only real eigenfrequencies, accompanied by a gap between all branches. The low-lying branch exhibits a phonon mode, as shown in Fig. 1(a i). The eigenspectrum is symmetric about the quasimomentum direction. To further explore the detailed nature of the excitations, we plot the eigenvectors corresponding to the eigenspectrum in Fig. 1(a i) in Figs. 1(a ii) and 1(a iii). Here we display three sets of eigenvector components, namely, $|u_{+1}|^2$, $|v_{+1}|^2$, $|u_0|^2$, $|v_0|^2$, $|u_{-1}|^2$, and $|v_{-1}|^2$, for a specific branch of the eigenspectrum. We find that all eigenvector components exhibit a densitylike mode consistent with the real eigenfrequencies observed, aligning with previous studies on spin-$\frac{1}{2}$ SOC BECs [39,60]. Additionally, these eigenvectors satisfy the following relations for the low-lying and first-excited branches:

$$|u_{+1}|^2_{ll} - |u_{-1}|^2_{ll} = 0, \quad |v_{+1}|^2_{ll} - |v_{-1}|^2_{ll} = 0,$$
$$|u_{+1}|^2_{fe} - |u_{-1}|^2_{fe} = 0, \quad |v_{+1}|^2_{fe} - |v_{-1}|^2_{fe} = 0. \qquad (9)$$

Apart from this, we find that the eigenvector components of the low-lying branch appear to approach the same value at $q_x \approx 0$, a typical feature of the phonon mode in the eigenspectrum [see Figs. 1(a ii) and 1(a iii)]. In Fig. 1(b i) we present the eigenfrequency for regime II ($k_L^2 > \Omega$) of the condensate, which clearly reveals the presence of imaginary eigenfrequencies in the low-lying and first-excited branches of the eigenspectrum, whereas the second-excited branch exhibits only real eigenfrequencies. The low-lying branch displays three instability bands at wave number and corresponding eigenfrequency pairs given by $\{q_x, \omega\} = \{0.33, 0.999\}$, $\{2.04, 0.799\}$, and $\{8.37, 0.773\}$, while the first-excited branch exhibits a single instability band at $q_x = 2.04$ with an eigenfrequency of $\omega = 0.799$. This single-band instability in the first-excited branch arises due to an UAC between the low-lying and first-excited branches of the eigenspectrum, occurring within the quasimomentum range $1.14 \lesssim q_x \lesssim 2.94$. This interaction is primarily responsible for the I_o-type dynamical instability [47–49]. The presence of imaginary eigenfrequencies indicates dynamical instability in the condensate phase. Similar to regime I, in regime II we also observe that the eigenspectrum is symmetric about the quasimomentum direction; however, it distinctly exhibits multiband instability. This multiband nature manifests in the eigenvectors as a spinlike mode, satisfying a specific relationship between the low-lying and first-excited branches of the excitation spectrum

$$|u_{+1}|_{ll}^2 - |u_{-1}|_{ll}^2 \neq 0, \quad |v_{+1}|_{ll}^2 - |v_{-1}|_{ll}^2 \neq 0,$$
$$|u_{+1}|_{fe}^2 - |u_{-1}|_{fe}^2 \neq 0, \quad |v_{+1}|_{fe}^2 - |v_{-1}|_{fe}^2 \neq 0. \quad (10)$$

The eigenvectors of the low-lying branch display an interesting feature of the transition from the spinlike mode to the densitylike mode, which indicates the presence of a transition $\text{Im}(\omega) \to \text{Re}(\omega)$, and then from the densitylike mode to the spinlike mode, which informs that $\text{Re}(\omega) \to \text{Im}(\omega)$ and in the weak wavelength limit only $\text{Re}(\omega)$ is present and $\text{Im}(\omega)$ is absent. This particular feature suggests the presence of the spin-density-spin mixed mode of the eigenvector in the three-instability-band regions of the eigenspectrum. The first-excited branch of the eigenspectrum has a single instability band that occurs due to the UAC between the low-lying and first-excited branches, which lies in the quasimomentum range $1.14 \lesssim q_x \lesssim 2.94$. Closer to the q_x of UAC, the eigenvectors of the low-lying and first-excited branches display out-of-phase behavior among the branches [see Fig. 1(b ii)]. However, the zeroth component of eigenvectors exhibits a densitylike mode only [see Fig. 1(b iii)].

After analyzing the collective excitation spectrum, we wish to understand the appearance of MI in the phase plots. Specifically, we focus on the k_L-q_x plane for the FM SOC BECs. In Figs. 2(a) and 2(b) we present the pseudocolor representation of the modulational instability gain, defined as the imaginary part of the modulus of eigenfrequency, for a Rabi coupling strength $\Omega = 1$ and with FM interaction strengths $c_0 = 5.0$ and $c_2 = -2.0$. We observe that instability bands start emerging in the range where $k_L^2 > \Omega$, first appearing in the low-lying branch Σ_{ll} as a single band. However, for $k_L > 3$ two instability band emerge and for $k_L > 4$ three bands are observed [see Fig. 2(a)]. For the first-excited branch Σ_{fe},
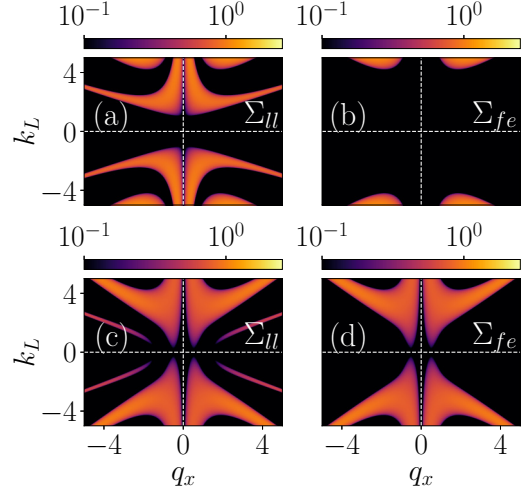

FIG. 2. Pseudocolor plot of the modulational instability gain for the ferromagnetic phase ($c_0 = 5$ and $c_2 = -2$) in the k_L-q_x plane for (a) and (b) $\Omega = 1$ and (c) and (d) $\Omega = -1$ in (a) and (c) $\Sigma_{ll} \equiv |\text{Im}(\omega_{ll})|$ and (b) and (d) $\Sigma_{fe} \equiv |\text{Im}(\omega_{fe})|$. In (a) multiband instability gain appears at $k_L = 1$ and in (b) a single-band instability appears at $k_L \approx 4.0$. In (c) and (d) double- and single-band instabilities appear at $k_L > 0.25$, respectively. The second-excited branch of the eigenspectrum shows the absence of instability gain for both sets of parameters. The instability gain is symmetric about k_L and q_x.

instability emerges only at higher values of the spin-orbit coupling ($k_L \gtrsim 4.0$). This can be attributed to the emergence of an UAC between the ω_{ll} and ω_{fe} branches within the quasimomentum range $0.95 < q_x < 3.64$. Initially, this forms a single instability band, which expands as the SOC strength increases. In Figs. 2(c) and 2(d) we present the MI gain for the low-lying and first-excited modes, respectively, at $\Omega = -1$, with all other parameters held constant as those used for $\Omega = 1$. Here we observe a markedly different trend compared to those results obtained with a positive Rabi frequency. In a spin-1 condensate, negative Rabi coupling increases the system's energy, manifesting as a higher number of instability bands [61]. For negative Rabi strength, we notice that the instability appears at a lower SOC value ($k_L > 0.25$) compared to that for positive Rabi strength [see Figs. 2(c) and 2(d)]. The instability manifests as double bands in the low-lying branch and a single band in the first-excited branch, both of which intensify with increasing SOC strength. The instability gain is symmetric about the quasimomentum q_x and the SOC strength k_L. Notably, the second-excited branch exhibits no instability gain in the FM BECs, even in the presence of spin-orbit coupling k_L. After getting a clear understanding of how Rabi coupling affects the MI gain in the k_L-q_x plane, we now shift our focus to exploring the same in the Ω-q_x plane by fixing the SOC strength as $k_L = 1$. We analyze the impact of Rabi coupling on the MI gain for the FM interaction strengths $c_0 = 5.0$ and $c_2 = -2.0$. To systematically investigate the impact of Rabi coupling strength on the eigenspectrum, we begin our analysis by choosing $k_L = 1.0$. We find that the low-lying branch of the eigenspectrum exhibits finite instability gain for $\Omega < 1$ [see Fig. 3(a)], but for $\Omega > 1$ the modes become stable. Upon examining the other two branches, namely, the first-excited branch and the second-excited branch, we
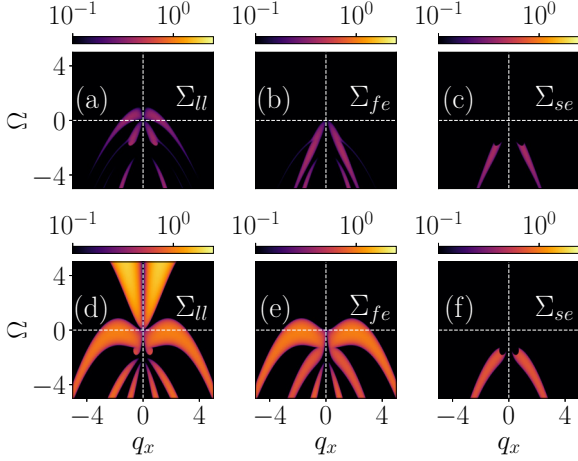
FIG. 3. Pseudocolor plot of the modulational instability gain in Ω-q_x phase plane for FM interactions ($c_0 = 5.0$ and $c_2 = -2.0$) for (a)–(c) $k_L = 1$ and (d)–(f) $k_L = 4.0$ in the (a) and (d) $\Sigma_{ll} \equiv |\text{Im}(\omega_{ll})|$, (b) and (e) $\Sigma_{fe} \equiv |\text{Im}(\omega_{fe})|$, and (c) and (f) $\Sigma_{se} \equiv |\text{Im}(\omega_{se})|$ low-lying, first-excited, and second-excited branches of the excitation spectrum, respectively. In (a) the primary band appears for $\Omega > 0$ following the relation $k_L^2 = \Omega$, while in (b) and (c) it appears only for $\Omega < 0$, with a cutoff in (c) at $\Omega \approx -1.66$. Similar to (a)–(c), the primary instability band in (d) appears for $\Omega > 0$. In (d) and (e) the secondary and primary bands appear for $\Omega > 0$, which is different than for (a)–(c). In (f) single-band instability appears for $\Omega < 0$, following a cutoff value $\Omega \approx -1.44$. The instability gain that appears is not symmetric about Ω and increases upon decreasing Ω; however, it shows symmetric behavior about q_x.

observe that the instability gain becomes finite only for $\Omega < 0$, as illustrated in Figs. 3(b) and 3(c), respectively. Interestingly, the low-lying and first-excited branches of the eigenspectrum display multiple instability bands for $\Omega < 0$, whereas the second-excited branch exhibits only a single instability band starting at $\Omega \lesssim -1.66$. Upon considering stronger SOC strength ($k_L = 4.0$), multiband instabilities appear in both the low-lying and the first-excited branches [see Figs. 3(d)–3(f)]. The second-excited branch, however, still only shows a single instability band, similar to the case with $k_L = 1$. Comparing the instability features across the range of Rabi frequencies from $-\Omega$ to $+\Omega$, we observe a transition from multiband instability to a single instability band in the low-lying branch, accompanied by the existence of a primary band in the first-excited branch for $\Omega > 0$. The primary instability band in the low-lying branch appears at $k_L^2 = \Omega$. In the second-excited branch, a single instability band is present for $\Omega \lesssim -1.44$. Furthermore, the instability gains Σ_{ll}, Σ_{fe}, and Σ_{se} in all three branches increase as the Rabi coupling strength decreases, and they exhibit symmetry about q_x.

Overall, we find that SOC BECs with FM interaction exhibit a single UAC between ω_{ll} and ω_{fe}, as previously reported [48]. This UAC emerges at critical values of coupling strength, following the relation $\Omega \approx 0.1278 k_L^2 - 1.1358$, with its origin at $(k_L, \Omega) = (2.94, 0.01)$. Interestingly, in MI analysis [9,42], we observe that for $\Omega < 0$, the first-excited branch ω_{fe} exhibits a second UAC with the second-excited branch ω_{se}, accompanied by the emergence of more multiband instabilities compared to cases where $\Omega > 0$.
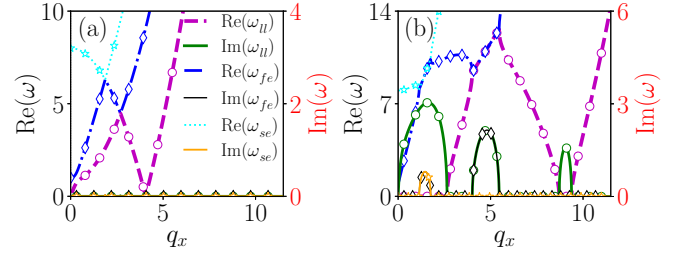

FIG. 4. Eigenspectrum with AFM interaction ($c_0 = 5.0$ and $c_2 = 5.0$) for (a) $(k_L, \Omega) = (0.5, 1.0)$ and (b) $(k_L, \Omega) = (4.5, 1.0)$. The lines and symbols have the same meaning as in Figs. 1(a i) and 1(b i). (a) A stable avoided crossing appears between the first-excited (ω_{fe}) and second-excited (ω_{se}) branches as well as between low-lying (ω_{ll}) and ω_{fe} branches. (b) As spin-orbit coupling is increased, multiband instability emerges in the eigenspectrum accompanied by the appearance of UACs between the ω_{fe} and ω_{se} branches and between the ω_{ll} and ω_{fe} branches. The first-excited branch exhibits the double UAC. The right vertical axis represents the imaginary eigenfrequencies.

After analyzing the collective excitation for FM interaction, we now present the corresponding analysis for the AFM interaction.

B. Collective excitation spectrum of AFM SOC BECs ($c_0 > 0$ and $c_2 > 0$)

In this section, we present the collective excitation spectrum for AFM interaction SOC BECs by considering $c_0 = c_2 = 5.0$. In regime I, with $k_L = 0.5$ and $\Omega = 1.0$, the eigenspectrum exhibits only real eigenfrequencies. However, avoided crossings occur between the ω_{ll} and ω_{fe} branches at $q_x \sim 2.70$ and between the ω_{fe} and ω_{se} branches at $q_x \sim 1.87$ [see Fig. 4(a)]. As the imaginary part of the eigenspectrum is zero $\text{Im}(\omega_j) = 0$, the condensate remains dynamically stable. The involvement of the first-excited branch in both of these stable avoided crossings results in a double stable avoided crossing near $q_x \sim 1.87$ and $q_x \sim 2.70$, as depicted in Fig. 4(a). Furthermore, the minimum of the low-lying excitation spectrum occurs at $q_x = 4.06$, corresponding to the phonon energy minimum. This minimum corresponds to the rotonic minimum and is responsible for the emergence of the plane-wave phase in spin-1 AFM SOC BECs [62,63]. Such features are not observed in FM SOC BECs.

In Fig. 4(b) we show the eigenspectrum corresponding to regime II, where we consider $k_L = 4.5$ and $\Omega = 1.0$. The other parameters are the same as those in Fig. 4(a). In this regime, we notice the appearance of a multiband imaginary eigenfrequency in both the ω_{ll} and ω_{fe} branches. There are three instability bands present in the low-lying branch, whose location and corresponding amplitude are given as $\{q_x, \omega\} = \{1.63, 3.037\}, \{4.81, 2.149\}, \{9.06, 1.585\}$. However, the other two instability bands appear in the first-excited branch with position and amplitudes $\{q_x, \omega\} = \{1.46, 0.802\}, \{4.81, 2.149\}$. Additionally, we notice the presence of a single-band instability in the ω_{se} branch with $\{q_x, \omega\} = \{1.46, 0.802\}$, which arises solely due to crossing between ω_{se} and ω_{fe}. The presence of imaginary eigenfrequency leads to dynamical instability in regime II,
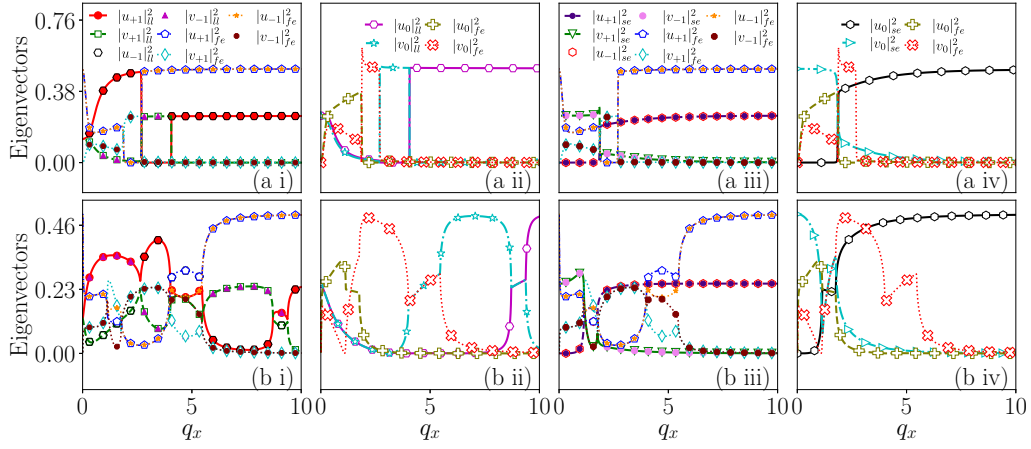
FIG. 5. (a) and (b) Eigenvectors corresponding to Figs. 4(a) and 4(b), respectively, for (i) and (ii) the low-lying and first-excited branches and (iii) and (iv) the second-excited and first-excited branches of the eigenspectrum. The eigenvectors of the low-lying branch are given as $|u_{+1}|^2_{ll}$ (red circles), $|u_{-1}|^2_{ll}$ (black hexagons), $|u_0|^2_{ll}$ (magenta hexagons), $|v_0|^2_{ll}$ (cyan open stars), $|v_{+1}|^2_{ll}$ (green open squares), and $|v_{-1}|^2_{ll}$ (magenta triangles) and for the first-excited branch as $|u_{+1}|^2_{fe}$ (blue open pentagons), $|u_{-1}|^2_{fe}$ (orange stars), $|u_0|^2_{fe}$ (olive open pluses), $|v_0|^2_{fe}$ (red open crosses with the dotted line), $|v_{+1}|^2_{fe}$ (cyan open diamonds), and $|v_{-1}|^2_{fe}$ (maroon closed circles). The eigenvectors of the second-excited branch are given as $|u_{+1}|^2_{se}$ (indigo circles), $|u_{-1}|^2_{se}$ (red hexagons), $|u_0|^2_{se}$ (black hexagons), $|v_0|^2_{se}$ (cyan right triangles), $|v_{+1}|^2_{se}$ (green open down triangles), and $|v_{-1}|^2_{se}$ (violet closed circles). (a) In-phase behavior (densitylike mode) with the occurrence of flip at the point of the stable avoided crossing between ω_{ll} and ω_{fe} and between ω_{se} and ω_{fe}. (b i) and (b iii) Out-of-phase behavior (spinlike mode). At the point of the UAC, eigenvectors are out of phase among the branches. (b ii) and (b iv) Only the densitylike mode.

as also obtained in [34,35,39]. The ω_{fe} branch experiences a double UAC, arising from avoided crossings with the other two branches. The first UAC between ω_{ll} and ω_{fe} appears in the quasimomentum range $4.01 \lesssim q_x \lesssim 5.49$, while the second UAC appears between ω_{fe} and ω_{se} in the quasimomentum range $1.14 \lesssim q_x \lesssim 1.78$ [see Fig. 4(b)]. Such an instability is responsible for an I_o-type dynamical instability [47,49], which will be discussed later in the paper.

Next we analyze the corresponding eigenvectors of regimes I and II for the AFM SOC BECs. In Fig. 5 we demonstrate the nature of eigenvectors corresponding to Fig. 4. First, we report for regime I the respective eigenspectrum presented in Fig. 4(a). As all the eigenfrequencies ω_{ll}, ω_{fe}, and ω_{se} are real, the corresponding eigenvector components display in-phase (densitylike) behavior in the quasimomentum direction q_x, which meets the criterion given in Eq. (9) (and also holds for the eigenvectors of the second-excited branch). A flip in the eigenvector components occurs at the point of the first stable avoided crossing around $q_x \sim 2.70$ between the ω_{ll} and ω_{fe} branches [see Fig. 5(a i)], similar to the result reported in Ref. [60]. As the second stable avoided crossing is observed between ω_{fe} and ω_{se}, the eigenvector components for corresponding branches also show the flipping tendency at the point of crossing at $q_x \sim 1.87$ [see Fig. 5(a iii)]. The zeroth component of eigenvectors of low-lying, first-excited, and second-excited branches of the eigenspectrum show a densitylike mode, which is given in Figs. 5(a ii) and 5(a iv). Overall, we observe that at the point of stable avoided crossing between the branches, the flip in eigenvectors of both branches occurs simultaneously at $q_x \approx 2.70$ and 1.87. Moreover, a further flip in the eigenvectors of the low-lying branch takes place at $q_x \approx 4.06$, when the eigenvalue spectrum approaches zero, where $\mathrm{Re}(\omega) = \mathrm{Im}(\omega) = 0$.

We present the nature of eigenvectors for high k_L corresponding to the eigenspectrum shown in Fig. 4(b). We

observe that, due to the presence of a complex eigenfrequency $[\mathrm{Im}(\omega_j) \neq 0]$, the eigenvector components show the spinlike (out-of-phase) behavior characterized by Eq. (10) (the same applied for the eigenvectors of the second-excited branch). As the low-lying and first-excited branches have multiband instability in the eigenspectrum, the eigenvectors exhibit a transition from the spinlike to the densitylike mode, resulting in a mixed mode. The first UAC between the ω_{ll} and ω_{fe} branches occurs in the quasimomentum range $4.01 \lesssim q_x \lesssim 5.49$ in the eigenspectrum [see Fig. 4(b)]; the corresponding eigenvectors exhibit complicated out-of-phase behavior among these branches, as illustrated in Fig. 5(b i). Looking at the eigenvector in the second UAC region ($1.14 \lesssim q_x \lesssim 1.78$), we find that the eigenvectors exhibit similar out-of-phase features [see Fig. 5(b iii)]. Interestingly, the zeroth components of the eigenvectors for the low-lying, first-excited, and second-excited branches exhibit the densitylike mode independently [see Figs. 5(b ii) and 5(b iv)] [48].

In the preceding section, we derived the multiband imaginary eigenfrequencies for the low-lying and first-excited branches, as well as the single-band imaginary eigenfrequency for the second-excited branch of the spectrum. The instability gains in these eigenspectra are characterized as $\Sigma_{ll,fe,se} = |\mathrm{Im}(\omega_{ll,fe,se})|$. After analyzing the presence of instability in the collective excitation spectrum of AFM SOC BECs, we aim to investigate the nature of this instability through instability gains using phase plots, varying the parameters k_L and Ω. We begin by examining the role of k_L (SOC strength) in the instability gain of AFM condensates with interaction strengths $c_0 = c_2 = 5.0$. In Figs. 6(a)–6(c) the Rabi coupling strength is fixed at $\Omega = 1$. Instability emerges when $k_L > 1$. In the low-lying branch Σ_{ll}, we observe the emergence of double-band instability along the quasimomentum direction. The growth of the primary instability increases with increasing SOC strength. Additionally, the bandwidth of
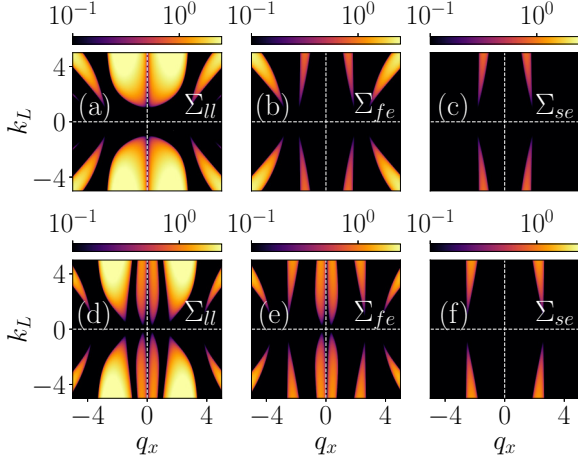
FIG. 6. MI gain in the k_L-q_x phase plane for (a)–(c) $\Omega = 1$ and (d)–(f) $\Omega = -1$. The interaction strengths are $c_0 = c_2 = 5.0$. The pseudocolor representation is the same as in Fig. 3. We obtain the instability bands (a)–(c) at $k_L = 1.0$, following the critical relation $k_L^2 = \Omega$, and (d)–(f) for $k_L > 0.25$. The symmetry arguments are similar to those in Fig. 2.

FIG. 7. MI gain in the Ω-q_x phase diagram for (a)–(c) $k_L = 1$ and (d)–(f) $k_L = 4.0$. Here the density-density interaction has $c_0 = 5.0$ and the spin-dependent interaction $c_2 = 5.0$. The pseudocolor bar is similar to that in Fig. 3. Multiband instability appears for the low-lying and first-excited branches of the spectrum, while the second-excited branch shows single-band instability. The instability gain is not symmetric about Ω and increases upon decreasing Ω; however, it shows symmetric behavior about q_x.

the secondary instability widens, exhibiting a hornlike shape. The first- and second-excited branches also display instability gains (Σ_{fe} and Σ_{se}), characterized by double- and single-band structures, respectively. For the instability gain of the first-excited state (Σ_{fe}), two humps appear: The primary instability band remains constant, while the secondary instability band expands with increasing SOC strength. The instability gain of the second-excited branch (Σ_{se}) and its bandwidth also exhibit an increasing trend as k_L increases. Interestingly, for a negative Rabi coupling ($\Omega = -1$), we observe a distinctly different trend compared to the positive Rabi coupling case. In a spin-1 system, negative Rabi coupling injects additional energy into the system [61], resulting in a higher number of instability bands. Consequently, instability arises earlier (at $k_L > 0.25$) compared to the positive Rabi coupling case [see Figs. 6(d)–6(f)]. Here triple instability bands appear in the low-lying and first-excited branches. The first band remains constant, while the bandwidth and instability gain of the second band vary with k_L, and the third band grows gradually with increasing spin-orbit-coupling strength, consistent with the previous case. For both $\Omega = 1$ and -1, the instability bandwidth of all branches remains symmetric about the quasi-momentum q_x and the spin-orbit-coupling strength k_L. Next we investigate the effect of Rabi coupling strength on the instability gain, denoted by $\Sigma_{ll,fe,se}$, in SOC spin-1 BECs with AFM interactions, where $c_0 = c_2 = 5$. In Figs. 7(a)–7(c) we fix the spin-orbit-coupling strength at $k_L = 1$ and vary the Rabi coupling strength Ω. This reveals double instability bands in the low-lying branch of the eigenspectrum, whereas the first-excited and second-excited branches exhibit only single-band instability. In the low-lying branch, the primary instability band emerges at $\Omega = 1.0$, increases in magnitude for $\Omega < 1.0$, and disappears, becoming stable for $\Omega > 1.0$. Additionally, a secondary instability band appears for $\Omega < 0$. In the first-excited branch, instability gain is observed for $\Omega < 0$, inheriting an UAC between the low-lying and
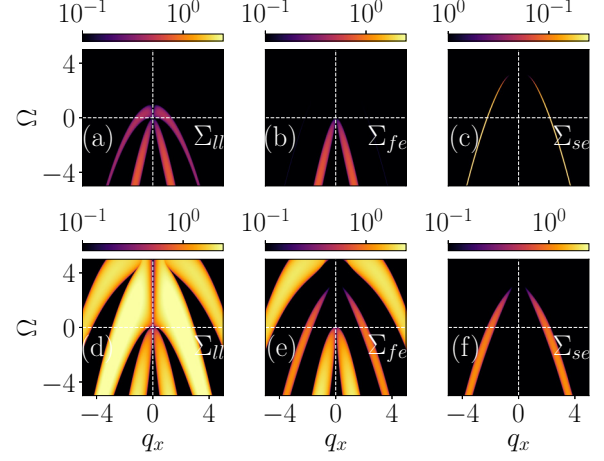
first-excited branches. In the second-excited branch, a single instability band emerges, growing for $\Omega \lesssim 3.15$; at $\Omega < 0$, a second UAC appears. Thus, when $\Omega < 0$, the AFM system exhibits double UACs and double instability gain bands [see Fig. 7(c)]. Note that as the amplitude of the instability gain for this branch is one order smaller than those of the other two branches, we multiply a factor of 20 to bring it to the same scale as the other two branches.

For a relatively strong spin-orbit-coupling strength of $k_L = 4.0$, we observe multiband instability in the low-lying and first-excited branches of the eigenspectrum, while the second-excited branch displays single-band instability for $\Omega < 3.0$. Due to the significantly higher SOC strength, the instability gain exhibits both a larger amplitude and higher coverage in the phase plane [see Figs. 7(d)–7(f)]. Comparing the two cases, we find that for weak spin-orbit coupling ($k_L = 1$), the maximum unstable phase occurs only for negative Ω, i.e., $-\Omega$, with stability observed for positive Ω, i.e., $+\Omega$. In contrast, for strong spin-orbit coupling ($k_L = 4.0$), the entire considered range of Ω is unstable.

In Fig. 7 the instability gain along the quasimomentum direction q_x increases as the Rabi coupling strength decreases, displaying symmetric behavior about q_x. Furthermore, we confirm that in regime II of the AFM interaction, double UACs are present for both positive and negative Ω ($\pm\Omega$), whereas in the FM interaction, double UACs occur only for negative Ω ($-\Omega$). Thus, both systems exhibit double UACs, with their appearance dependent on the Rabi coupling strength.

Further, we study the behavior of the system at fixed interaction strengths c_0 and c_2 and quasimomentum q_x, upon simultaneous varying the spin-orbit coupling (k_L) and Rabi coupling (Ω) strengths [see Figs. 8(a) and 8(b)]. We demonstrate the instability gain of the low-lying branch of the
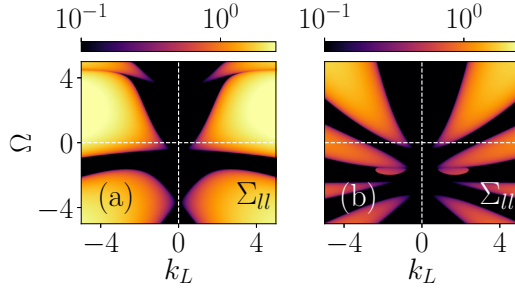
FIG. 8. Pseudocolor representation of the MI gain for $\Sigma_{ll} \equiv |\text{Im}(\omega_{ll})|$ in the k_L-Ω phase plane for (a) $(c_0, c_2) = (5, 5)$ and (b) $(c_0, c_2) = (5, -2)$ at quasimomentum $q_x = 1$. Multiband instability appears in each case, which increases upon increasing k_L. The instability bands show symmetric behavior about k_L; however, it is not symmetric with the variation in Ω.

FIG. 9. (a) Pseudocolor representation of the MI gain for the low-lying mode $\Sigma_{ll} \equiv |\text{Im}(\omega_{ll})|$ in the c_0-q_x phase plane with $(k_L, \Omega) = (0.5, 1.0)$. Also shown is the pseudocolor representation of the MI gain for (b) the low-lying mode $\Sigma_{ll} \equiv |\text{Im}(\omega_{ll})|$ and (c) the first-excited mode $\Sigma_{fe} \equiv |\text{Im}(\omega_{fe})|$ in the c_0-q_x phase plane for $(k_L, \Omega) = (4.5, 1.0)$. The spin-exchange interaction is $c_2 = -2.0$. In (a), the instability gain appears only in the low-lying branch, while in (b) and (c) it appears in the low-lying and first-excited branches of the excitation spectrum. The instability gain increases upon decreasing c_0, showing symmetric behavior about q_x; however, it is not symmetric about c_0.

eigenspectrum corresponding to two different sets of interaction strengths at $q_x = 1$. In Fig. 8(a) we consider interaction strengths corresponding to AFM interaction and in Fig. 8(b) corresponding to FM interaction. We obtain multiband instability for both cases, which is not symmetric about Ω. The instability gain is symmetric about k_L and increases upon increasing the spin-orbit-coupling strength. Here we conclude that regime I ($\Omega > k_L^2$) is dynamically stable, while regime II ($\Omega < k_L^2$) is dynamically unstable and exhibits multi-instability bands. Moreover, with respect to the negative Rabi couplings, both spinor BECs exhibit double UACs. Additionally, we observe that the instability gain of the FM condensate is reduced by approximately half for the AFM condensate, indicating that the latter is dynamically more unstable and sensitive to perturbations.

IV. IMPACT OF DENSITY-DENSITY INTERACTION AND SPIN-EXCHANGE INTERACTION ON THE MI

So far we have analyzed the effect of k_L and Ω on the collective excitation spectrum for the FM $(c_0, c_2) = (5.0, -2.0)$ and AFM $(c_0, c_2) = (5.0, 5.0)$ interaction phases of the SOC spin-1 condensate. For FM interactions, the instabilities mainly appear in the low-lying and first-excited branches of the eigenspectrum. However, for AFM interactions, they appear in the low-lying, first-excited, and second-excited branches. Next, to make our analysis more general, we scan a wide range of interactions ($(c_2, c_0) \in [-10, 10]$) for low-spin-orbit-coupling ($k_L^2 < \Omega$) and high-spin-orbit-coupling ($k_L^2 > \Omega$) regimes.

First, we consider the effect of the density-density interaction term c_0 by choosing c_2 positive or negative. At first, we choose $c_2 = -2.0$ along with two different sets of coupling strengths k_L and Ω. For $k_L^2 < \Omega$, we find that the instability gain is zero as long as the total interaction strength remains repulsive, i.e., $c_0 + c_2 > 0$. However, single-band instability appears in the low-lying branch of the eigenspectrum when the total interaction strength is attractive, i.e., $c_0 + c_2 < 0$. For $c_2 = -2.0$ and $c_0 > 2.0$, the instability gain is absent. The instability appears where the interaction follows the relation $c_0 + c_2 < 0$. The instability gain appears to increase upon further decreasing c_0 [see Fig. 9(a)]. However, there is a lack
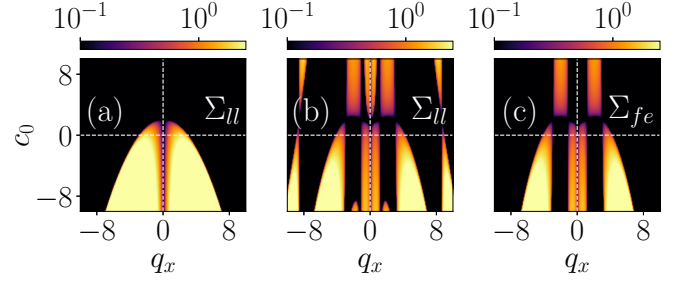
of instability in the first- and second-excited branches (not shown here). Now we consider regime II, where $k_L^2 > \Omega$, and we obtain multiband instability that appears in the low-lying and first-excited branches of the spectrum. The instability gain of the spectrum increases upon decreasing c_0 [see Figs. 9(b) and 9(c)]. On the other hand, instability gain is absent in the second-excited branch of the eigenspectrum. We find that regime I has instability only for the attractive system and no UAC, but regime II is stable only for $c_0 + c_2 \approx 0$ and otherwise exhibits UAC but no appearance of double UACs. For both sets of coupling strengths, the instability gain of the spectrum is symmetric about q_x and not symmetric about c_0. In the above, we analyzed the effect of c_0 in the presence of $c_2 = -2.0$. Further, to analyze the impact of positive interaction, we consider $c_2 = 5.0$. Here also we consider the low-k_L regime, regime I ($k_L^2 < \Omega$), and the high-k_L regime, regime II ($k_L^2 > \Omega$). For regime I, we consider c_0 in the range $[-5, 5]$ and obtain only real eigenfrequencies in the eigenspectrum. Therefore, the instability gain remains absent and is responsible for the dynamical stable phases (not shown here). Further, we choose regime II, which exhibits multiband instability that appears in the low-lying and first-excited branches of the eigenspectrum [see Figs. 10(a) and 10(b)], while the second-excited branch shows single-band instability [see Fig. 10(c)]. Regime II is stable only for the attractive c_0 interactions results as $c_0 + c_2 \approx 0$. The instability gain increases upon increasing c_0, showing symmetric behavior about q_x, while it is not symmetric about c_0.

After exploring the density-density interaction parameter regime, we now shift our focus to analyzing the impact of the spin-exchange interaction strength c_2 on the instability while keeping the density-density interaction strength fixed at $c_0 = 5.0$. In regime I, we consider c_2 in the range $[-5, 5]$, and the eigenspectrum yields only real eigenfrequencies, indicating an absence of instability (not shown here). In contrast, for regime II, we observe the emergence of multiband instability in both the low-lying and first-excited branches of
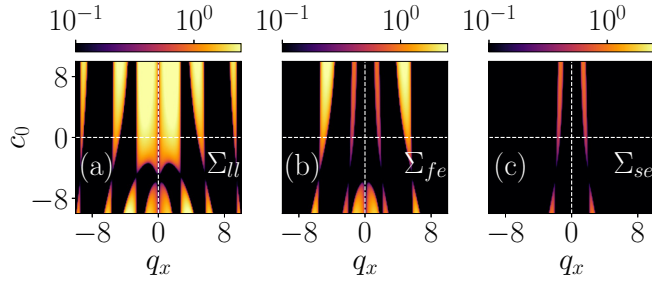
FIG. 10. MI of the AFM interaction ($c_2 = 5.0$) in the c_0-q_x phase plane for $k_L = 4.5$ and $\Omega = 1.0$. The pseudocolor bar is similar to that in Fig. 3. Multiband instability in the (a) low-lying and (b) first-excited branches and (c) single-band instability in the second-excited branch of the eigenspectrum increase upon increasing c_0, with symmetry arguments similar to those in Fig. 9.

the eigenspectrum. The low-lying branch remains unstable across the considered range of c_2 (except where $c_0 + c_2 \approx 0$), while the first-excited branch exhibits instability accompanied by the first UAC. Conversely, the second-excited branch displays single-band instability when the effective interaction is AFM, coinciding with the appearance of a second UAC in the system, but only for $c_2 > 2$ [see Figs. 11(a)–11(c)]. The instability gain increases upon increasing c_2, showing symmetric behavior about q_x, preserving asymmetric behavior about c_2.

In Fig. 12(a) we show the instability gain of the eigenspectrum upon simultaneously varying the density-density interaction strength c_0 and spin-exchange interaction strength c_2 for $(k_L, \Omega) = (0.5, 1.0)$. We find that the instability only occurs for the low-lying branch of the eigenspectrum for attractive interaction when $c_0 + c_2 < 0$. However, for the repulsive case ($c_0 + c_2 > 0$) the system appears to be stable. In Fig. 12(b) we show the instability gain corresponding to the low-lying eigenspectrum for $k_L = 4.0$ and $\Omega = 1.0$. For this case, we find the presence of a wider instability region in the entire range of interaction strengths, including both attractive and repulsive, as well as for the mixed case. Interestingly, we find that, for the mixed case of interactions, the system gets stabilized. Overall, we find that for the repulsive case, regime II shows instability; however, for regime I,
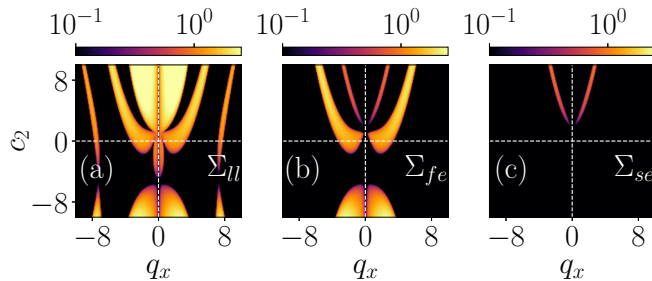

FIG. 11. MI in the c_2-q_x phase plane for $k_L = 4.0$ and $\Omega = 1.0$, with $c_0 = 5.0$. The pseudocolor bar is similar to that in Fig. 3. The instability gain of the spectrum increases upon increasing c_2, showing symmetric behavior about q_x; however, it is not symmetric about c_2.
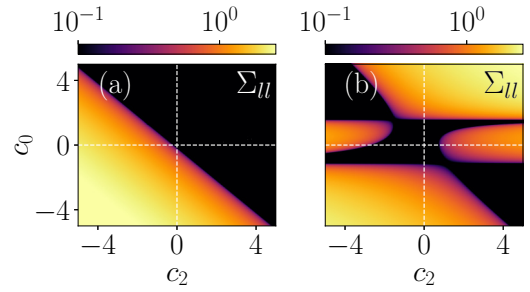

FIG. 12. Pseudocolor representation of the MI gain of the lowest eigenmode $\Sigma_{ll} \equiv |\text{Im}(\omega_{ll})|$ in the c_0-c_2 phase plane for (a) $(k_L, \Omega) = (0.5, 1.0)$ and (b) $(k_L, \Omega) = (4.0, 1.0)$. The quasimomentum strength is fixed at $q_x = 1$. In (a) the instability gain appears only in the low-lying branch when the total interaction strength is attractive $c_0 + c_2 < 0$, while in (b) the spectrum exhibits multiband instability. The instability gain in the eigenspectrum is not symmetric about c_0 or about c_2.

the repulsive interaction shows a stable nature. The instability gain of the eigenspectrum is not symmetric about c_0 or c_2.

V. CHARACTERIZATION OF DOUBLE UNAVOIDED CROSSINGS USING THE BAND GAPs Δ_{g1} AND Δ_{g2} OF THE EIGENSPECTRUM

After gaining a comprehensive understanding of the instability of FM and AFM interactions, we now characterize the band gap between the eigenbranches. The band gaps in the eigenspectrum are defined as the difference between the first-excited and low-lying states, expressed as $\Delta_{g1} = \text{Re}(\omega_{fe}) - \text{Re}(\omega_{ll})$, and the difference between the second-excited and first-excited states, expressed as $\Delta_{g2} = \text{Re}(\omega_{se}) - \text{Re}(\omega_{fe})$. A value of $\Delta_{g1} \sim 0$ indicates the presence of a gapless mode between ω_{ll} and ω_{fe}, while $\Delta_{g2} \sim 0$ signifies a gapless mode between ω_{fe} and ω_{se}.

In this study, we fix the density-density interaction at $c_0 = 5$ and the Rabi coupling at $\Omega = 1$, while varying the spin-orbit-coupling strength as $k_L = 0.5$ (regime I), 2.0, and 4.5 (regime II), as shown in Figs. 13(a)–13(c), respectively. Figures 13(a i) and 13(a ii) demonstrate that, when simultaneously varying the spin-exchange interaction c_2 and quasimomentum q_x with a fixed $c_0 = 5$, no band gap exists ($\Delta_{g1} = \Delta_{g2} = 0$) only for $c_2 > 0$ (AFM interactions). This gapless state persists as c_2 increases, indicating no gap between ω_{fe} and ω_{ll} and between ω_{se} and ω_{fe}. Conversely, for $c_2 < 0$ (FM interactions), only gapped modes are observed between all branches.

Similarly, upon increasing the spin-orbit-coupling strength to $k_L = 2.0$, the band gaps close only for $c_2 > 0$, with the gapless region expanding in the $c_2 - q_x$ plane and maintaining its gapless nature as c_2 increases [see Figs. 13(b i) and 13(b ii)]. Next we consider a relatively large spin-orbit-coupling strength of $k_L = 4.5$. In this case, the first UAC appears with $\Delta_{g1} = 0$ between the low-lying and first-excited branches only for $-2 < c_2 < 0$ (FM case), consistent with findings in SOC spin-1 ferromagnetic BECs [48]. This first UAC persists even in the $c_2 > 0$ regime [see Fig. 13(c i)]. However, a second UAC emerges for $c_2 > 0$ [see Fig. 13(c ii)].
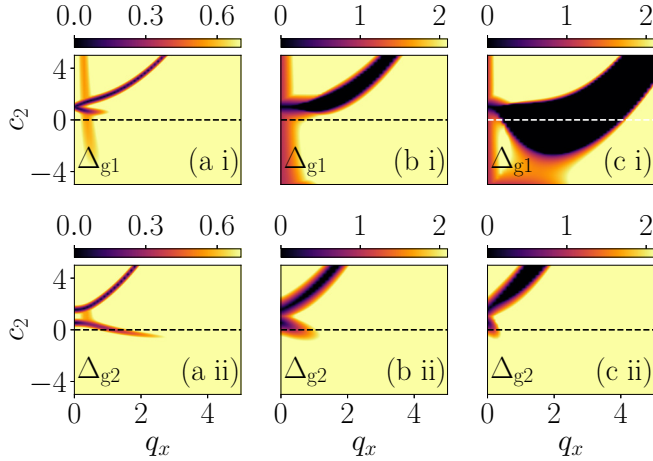
FIG. 13. Pseudocolor representation of the changes in band gap $\Delta_{g1} = \mathrm{Re}(\omega_{fe}) - \mathrm{Re}(\omega_{ll})$ and $\Delta_{g2} = \mathrm{Re}(\omega_{se}) - \mathrm{Re}(\omega_{fe})$ for different k_L in the c_2-q_x plane by keeping $\Omega = 1.0$ and $c_0 = 5.0$ for (a i) and (a ii) $k_L = 0.5$, (b i) and (b ii) $k_L = 2.0$, and (c i) and (c ii) $k_L = 4.5$. In (a i) and (b i), the band gap Δ_{g1} closes for positive $c_2 > 0$ (AFM interaction); however, in (c i) it closes for both AFM ($c_2 > 0$) and FM ($c_2 < 0$) interactions. In (a ii)–(c ii) the band gap Δ_{g2} closes for AFM interactions only ($c_2 > 0$).

Thus, a relatively strong spin-orbit coupling exhibits two gapless UACs when $c_2 > 0$, whereas a single gapless UAC occurs for $-2 < c_2 < 0$.

In conclusion, in regime II, ferromagnetic SOC BECs exhibit a single UAC, while AFM interactions result in double UACs between the branches. In contrast, regime I remains stable, displaying two gapless stable avoided crossings for $c_2 > 0$ and only gapped modes for $c_2 < 0$.

VI. NUMERICAL SIMULATION

In this section, we present the numerical simulation results to understand the nature of the dynamical stability of the condensate. We obtain the ground state of the condensate using the imaginary-time propagation (ITP) method and then evolve it using the real-time propagation (RTP) method by quenching the trap strength. We use the split-step Crank-Nicolson scheme to implement both ITP and RTP methods [19,20]. We consider a space grid $[-32, 32]$ with the space step $dx = 0.05$ in both ITP and RTP. The considered time steps are $dt = 0.00025$ and 0.0005 for ITP and RTP, respectively. Here we choose two quantum phases in the two different SOC BECs, namely, FM and AFM BECs.

A. Dynamics of ferromagnetic SOC BECs

In this section, we present the dynamics of the ground state for the two regimes of the ferromagnetic SOC BECs.

For regime I ($k_L = 0.5$ and $\Omega = 1.0$), we generate the plane-wave (PW) phase of the FM interaction ground-state phase using the parameters $c_0 = 5.0$, $c_2 = -2.0$, $k_L = 0.5$, and $\Omega = 1.0$ under a harmonic trap with strength $\lambda = 0.10$. After obtaining the ground state, we apply an instantaneous quench in the trap strength, triggering the dynamics of the condensate, which are computed using real-time propagation.
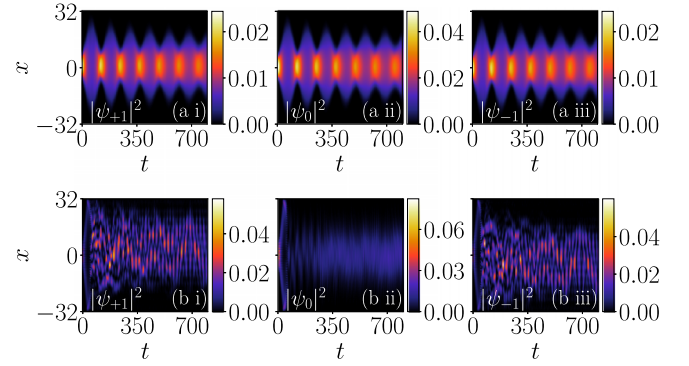

FIG. 14. Time evolution of the condensate in the x-t plane for the $|\psi_{+1}|^2$, $|\psi_0|^2$, and $|\psi_{-1}|^2$ components of the condensate for (a) $(k_L, \Omega) = (0.5, 1.0)$ and (b) $(k_L, \Omega) = (4.5, 1.0)$, upon quenching the trap strength to one-third of its initial value. The interaction strengths are $c_0 = 5.0$ and $c_2 = -2.0$. In (a) the density profile shows stable behavior throughout, showing the dynamical stability of the condensate. In (b) the density profile holds its SW nature for a while; at a later time, $|\psi_{\pm1}|^2$ fragments in small domains and shows a decay in amplitude while the zeroth component diminishes at first and then increases the amplitude.

In Figs. 14(a i)–14(a iii) we present the dynamical evolution of the density profiles for the three components of the condensate, revealing breathing oscillations. This characteristic response of the condensate to perturbation confirms the real eigenfrequency for these parameters, as illustrated in Fig. 1(a). For regime II ($k_L = 4.5$ and $\Omega = 1.0$), we obtain the ground state with the interaction strength $c_0 = 5.0$ and $c_2 = -2.0$ and considering spin-orbit coupling and Rabi coupling strength as $k_L = 4.5$ and $\Omega = 1.0$, respectively, which is a stripe-wave (SW) phase. Further, in time evolution, perturbing the trap strength of the density profile of the condensate changes its shape and amplitude. Here we discuss it in the x-t plane. The density profile evolves as the stripe wave in the beginning, but for $t > 0$, densities $|\psi_{\pm1}|^2$ fragment into several small domains, while the zeroth component density diminishes up to $t \approx 400$, and afterward $|\psi_0|^2$ has very weak growth; for $t > 400$, all the components exhibit an immisciblelike nonlinear wave pattern. Moreover, we find that in the absence of magnetization ($m = 0$), the condensates remain polarized in the $\pm x$ directions, which is not observed in regime I [see Figs. 14(b i)–14(b iii)] [48,64], due to the appearance of instability, as shown in Fig. 1(b). Overall, we find that the numerical simulation confirms the dynamical instability of the condensate, which is in line with the collective excitation spectrum calculation.

B. Dynamics of antiferromagnetic SOC BECs

First, we consider the dynamics of regime I ($k_L = 0.5$ and $\Omega = 1.0$), which also yields the PW phase of the AFM interaction of the SOC BECs. Initially, we generate the ground state with equal interaction strengths $c_0 = 5.0$ and $c_2 = 5.0$, keeping the Rabi coupling and spin-orbit coupling as $\Omega = 1.0$ and $k_L = 0.5$, respectively. We then generate the dynamics of the condensate by quenching the trap strength. The dynamical evolution of the condensate is obtained by using the RTP of
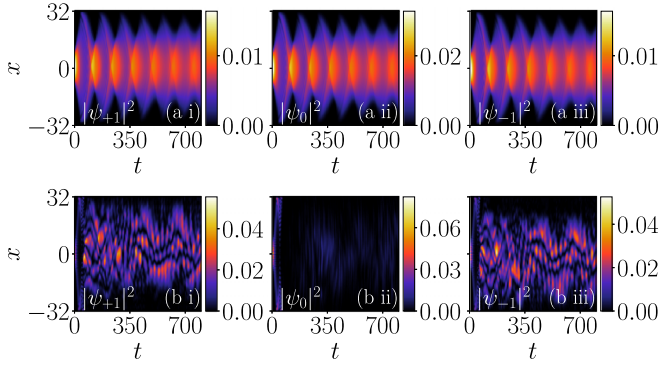
FIG. 15. Dynamical evolution of the condensate in the *x-t* plane for the $|\psi_{+1}|^2$, $|\psi_0|^2$, and $|\psi_{-1}|^2$ components of the condensate for (a) $k_L = 0.5$ and $\Omega = 1.0$ and (b) $k_L = 4.5$ and $\Omega = 1.0$, by quenching the trap strength to one-third of its initial value. The interaction strengths are $c_0 = 5.0$ and $c_2 = 5.0$. In the PW phase, the density of the condensate shows stable breatherlike dynamics. The SW phase holds its shape in the beginning, then the $|\psi_{\pm1}|^2$ components fragment into several small domains, and the zeroth components start diminishing, confirming the dynamical instability of the condensate.

the GPE. In Figs. 15(a i)–15(a iii) we show the densities of the three component $|\psi_{+1}|^2$, $|\psi_0|^2$, and $|\psi_{-1}|^2$, respectively. During temporal evolution, the density shows stable breather oscillation. This particular feature of the condensate complements the real nature of the collective excitation spectrum corresponding to this regime as presented in Fig. 4(a). This constant behavior of the density profile during dynamical evolution and stable energy complements the dynamically and energetically stable nature of the condensate.

In Figs. 15(b i)–15(b iii) we show the dynamical evolution of the density component for regime II ($k_L = 4.5$ and $\Omega = 1.0$) attained after the quench of potential strength for the ground state prepared with interaction strengths $c_0 = 5.0$ and $c_2 = 5.0$. We find that the density profile, which has a stripe-wave nature for all the components at $t = 0$, starts getting fragmented into several small domains upon evolution. While ±1 components get polarized [see Figs. 15(b i) and 15(b iii)], the zeroth component density starts diminishing [see Fig. 15(b ii)] [44,46,65]. This particular dynamical feature of the condensate complements the presence of the double UAC, which are present with both low-lying and second-excited branches, resulting in I_o-type instabilities and thus making the condensate dynamically unstable. It is worth noting that a similar domain formation has been realized in the presence of a weak Zeeman coupling [46].

VII. CONCLUSION

We have studied the stability of various phases in spin-orbit-coupled spin-1 SOC BECs with FM and AFM interactions. The Bogoliubov–de Gennes theory was employed to compute the eigenspectrum of the condensate.

For ferromagnetic interactions in the low-spin-orbit-coupling regime ($k_L^2 < \Omega$), the eigenspectrum exhibits real eigenfrequencies with a gap between the branches, showing phonon modes in the low-lying branch. The eigenvectors corresponding to the low-lying branch components approach

the same value at $q_x \approx 0$, confirming the presence of phonon modes. In the high-spin-orbit-coupling regime ($k_L^2 > \Omega$), we observe multiband imaginary eigenfrequencies in the low-lying branch. For FM interactions, we find the emergence of an UAC between the low-lying and first-excited branches, indicating the presence of I_o-type instability in each branch. The eigenvectors in this regime exhibit spin-density-like mixed modes arising from the multiband eigenfrequencies in quasi-momentum space. At the wave-number regime where UAC occurs, the eigenvector shows out-of-phase behavior for all the components of the condensate.

For AFM interactions with low-spin-orbit coupling, we observe stable avoided crossings between the low-lying and first-excited branches, as well as between the first- and second-excited branches. At these stable avoided crossings, the eigenvectors of all components display flipping characteristics. In the high-spin-orbit-coupling regime ($\Omega < k_L^2$), we identify multiband imaginary eigenfrequencies in the low-lying and first-excited branches, accompanied by single-band instability in the second-excited branch. Evidence of I_o-type instability is observed in the excitation spectrum, primarily originating from the first UAC between the low-lying and first-excited branches and the second UAC between the first- and second-excited branches. Notably, for AFM interactions, the first-excited branch exhibits a double UAC, a feature not present in the ferromagnetic case. The eigenvectors for AFM interactions reveal spin-density-like mixed modes in the low-lying and first-excited branches, while the second-excited branch transitions from density to spin modes due to single-band instability. The presence of an UAC and a double UAC induces out-of-phase behavior in the respective components.

Further investigation into instability in momentum space reveals that while the instability region is symmetric in the spin-orbit-coupling range, it shows an asymmetric character in the Rabi coupling plane. For fixed values of Rabi coupling (positive or negative), both FM and AFM SOC BECs are destabilized only for high spin-orbit coupling ($k_L^2 > \Omega$). In the case of weak spin-orbit coupling in AFM BECs, instability and UACs are observed within the range $\Omega < 3$, while the system remains stable otherwise. In contrast, the FM condensate remains stable in this regime. Both systems exhibit a double UAC when $\Omega \lesssim 0$. For higher spin-orbit coupling, AFM interactions show an UAC for $\Omega \gtrsim 6$, with a double UAC appearing for $\Omega \lesssim 3$. The ferromagnetic condensate, however, remains unstable throughout the entire Rabi coupling range, with an UAC observed for $\Omega \lesssim 1$ and a double UAC for $\Omega \lesssim -2$. In the k_L-Ω phase plane, both systems exhibit stability only in regime I; instability prevails in all other regimes, driven by the spin-orbit-coupling strength and multiband instability. Finally, we have investigated the variation of the band gaps between low-lying excitation branches in the interaction parameter space, noting that AFM SOC BECs consistently showed double UACs, while ferromagnetic interactions displayed single UACs in the eigenspectrum.

We have complemented the dynamical stability of the condensate obtained using the BdG analysis through the mean-field GPEs for both the low-spin-orbit-coupling regime (regime I) and high-spin-orbit-coupling regime (regime II). For low spin-orbit coupling, we have reported the stable breather pattern of the condensate with FM and AFM

interactions, which very well complement the dynamically stable nature of the condensate as shown using the BdG analysis. At high spin-orbit coupling, for which the ground state is of stripe-wave phase nature, dynamically fragmented condensate is exhibited upon evolution for both interactions. This fragmentation is more pronounced in the AFM interaction, which may be attributed to the presence of instabilities across all branches. In AFM SOC BECs, the fragmentation is accompanied by the complex domain formation in which the amplitude of the component remains unchanged but the shape of the condensate fluctuates. In contrast, for FM SOC BECs, decay appears in the density profile, evidenced by the reduced amplitude and immiscibility of the condensates.

It would be intriguing to extend the present work to higher (two and three) dimensions, where SOC BECs can exhibit a diverse range of interesting topological and supersolid states [5,66]. Recently, it has been reported that the inclusion of the quadratic Zeeman term becomes a handy tool to tune the gap between the double roton minima, which in turn is helpful in inducing the plane wave to stripe phase transition in spin-1 SOC thermal BECs [67]. It would be interesting to explore the effect of the quadratic Zeeman term on all sorts of MI and low-lying excitation investigated in the present work. Controlling the gap between the low-lying excited state presented in the paper could be valuable for developing novel quantum material and technology using ultracold atomic systems.

DATA AVAILABILITY

The data that support the findings of this article are openly available [68], embargo periods may apply.

APPENDIX: RELEVANT TERMS OF THE BDG MATRIX OF COLLECTIVE EXCITATIONS

In this Appendix, we provide an explicit form of the matrix elements of the BdG matrix equation (6). The matrix elements of Eq. (6) read

$$H_+ = \frac{q_x^2}{2} + c_0\big(2\phi_{+1}^2 + \phi_0^2 + \phi_{-1}^2\big) + c_2\big(2\phi_{+1}^2 + \phi_0^2 - \phi_{-1}^2\big), \tag{A1}$$

$$H_0 = \frac{q_x^2}{2} + c_0\big(\phi_{+1}^2 + 2\phi_0^2 + \phi_{-1}^2\big) + c_2\big(\phi_{+1}^2 + \phi_{-1}^2\big), \tag{A2}$$

$$H_- = \frac{q_x^2}{2} + c_0\big(\phi_{+1}^2 + \phi_0^2 + 2\phi_{-1}^2\big) + c_2\big(2\phi_{-1}^2 + \phi_0^2 - \phi_{+1}^2\big), \tag{A3}$$

$$\mu_+\phi_{+1} = c_0\big(\phi_{+1}^2 + \phi_0^2 + \phi_{-1}^2\big)\phi_{+1} + c_2\big(\phi_{+1}^2 + \phi_0^2 - \phi_{-1}^2\big)\phi_{+1} + c_2\phi_0^2\phi_{-1}^* + \frac{\Omega}{\sqrt{2}}\phi_0, \tag{A4}$$

$$\mu_0\phi_0 = c_0\big(\phi_{+1}^2 + \phi_0^2 + \phi_{-1}^2\big)\phi_0 + c_2\big(\phi_{+1}^2 + \phi_{-1}^2\big)\phi_0 + 2c_2\phi_0^*\phi_{+1}\phi_{-1} + \frac{\Omega}{\sqrt{2}}(\phi_{+1} + \phi_{-1}), \tag{A5}$$

$$\mu_-\phi_{-1} = c_0\big(\phi_{+1}^2 + \phi_0^2 + \phi_{-1}^2\big)\phi_{-1} + c_2\big(\phi_{-1}^2 + \phi_0^2 - \phi_{+1}^2\big)\phi_{-1} + c_2\phi_0^2\phi_{+1}^* + \frac{\Omega}{\sqrt{2}}\phi_0, \tag{A6}$$

$$\mathcal{L}_{12} = C^+\phi_{+1}^2, \quad \mathcal{L}_{13} = C^+\phi_0^*\phi_{+1} - \frac{k_L}{\sqrt{2}}iq_x + 2c_2\phi_0\phi_{-1}^* + \frac{\Omega}{\sqrt{2}}, \quad \mathcal{L}_{14} = C^+\phi_0\phi_{+1},$$

$$\mathcal{L}_{15} = C^-\phi_{-1}^*\phi_{+1}, \quad \mathcal{L}_{16} = C^-\phi_{-1}\phi_{+1} + c_2\phi_0^2, \quad \mathcal{L}_{21} = -C^+\phi_{+1}^{*2}, \quad \mathcal{L}_{23} = -C^+\phi_0^*\phi_{+1}^*,$$

$$\mathcal{L}_{24} = -C^+\phi_0\phi_{+1}^* + \frac{k_L}{\sqrt{2}}iq_x - 2c_2\phi_0^*\phi_{-1} - \frac{\Omega}{\sqrt{2}}, \quad \mathcal{L}_{25} = -C^-\phi_{-1}^*\phi_{+1}^* - c_2\phi_0^{*2},$$

$$\mathcal{L}_{26} = -C^-\phi_{-1}\phi_{+1}^*, \quad \mathcal{L}_{31} = C^+\phi_{+1}^*\phi_0 + 2c_2\phi_0^*\phi_{-1} + \frac{k_L}{\sqrt{2}}iq_x + \frac{\Omega}{\sqrt{2}}, \quad \mathcal{L}_{32} = C^+\phi_{+1}\phi_0,$$

$$\mathcal{L}_{34} = c_0\phi_0^2 + 2c_2\phi_{+1}\phi_{-1}, \quad \mathcal{L}_{35} = C^+\phi_{-1}^*\phi_0 + 2c_2\phi_0^*\phi_{+1} - \frac{k_L}{\sqrt{2}}iq_x + \frac{\Omega}{\sqrt{2}}, \quad \mathcal{L}_{36} = C^+\phi_{-1}\phi_0,$$

$$\mathcal{L}_{41} = -C^+\phi_{+1}^*\phi_0^*, \quad \mathcal{L}_{42} = -C^+\phi_{+1}\phi_0^* - \frac{k_L}{\sqrt{2}}iq_x - 2c_2\phi_0\phi_{-1}^* - \frac{\Omega}{\sqrt{2}}, \quad \mathcal{L}_{43} = -c_0\phi_0^{*2} - 2c_2\phi_{+1}^*\phi_{-1}^*,$$

$$\mathcal{L}_{45} = -C^+\phi_{-1}^*\phi_0^*, \quad \mathcal{L}_{46} = -C^+\phi_{-1}\phi_0^* + \frac{k_L}{\sqrt{2}}iq_x - 2c_2\phi_0\phi_{+1}^* - \frac{\Omega}{\sqrt{2}}, \quad \mathcal{L}_{51} = C^-\phi_{+1}^*\phi_{-1},$$

$$\mathcal{L}_{52} = C^-\phi_{+1}\phi_{-1} + c_2\phi_0^2, \quad \mathcal{L}_{53} = C^+\phi_0^*\phi_{-1} + \frac{k_L}{\sqrt{2}}iq_x + 2c_2\phi_0\phi_{+1}^* + \frac{\Omega}{\sqrt{2}}, \quad \mathcal{L}_{54} = C^+\phi_0\phi_{-1},$$

$$\mathcal{L}_{56} = C^+\phi_{-1}^2, \quad \mathcal{L}_{61} = -C^-\phi_{+1}^*\phi_{-1}^* - c_2\phi_0^{*2}, \quad \mathcal{L}_{62} = -C^-\phi_{+1}\phi_{-1}^*, \quad \mathcal{L}_{63} = -C^+\phi_0^*\phi_{-1}^*,$$

$$\mathcal{L}_{64} = -C^+\phi_0\phi_{-1}^* - \frac{k_L}{\sqrt{2}}iq_x - 2c_2\phi_0^*\phi_{+1} - \frac{\Omega}{\sqrt{2}}, \quad \mathcal{L}_{65} = -C^+\phi_{-1}^{*2}.$$

Also,

$$C^+ \equiv c_0 + c_2, \quad C^- \equiv c_0 - c_2.$$

The coefficients for the BdG characteristic equation (8) are

$$b = -5\Omega^2 - 4c_2^2 - (2k_L^2 + 3\Omega + c_0)q_x^2 - \tfrac{3}{4}q_x^4 + c_2(8\Omega + q_x^2), \tag{A7}$$

$$\begin{aligned}
c = {} & 4\Omega^4 + \Omega\big[2\Omega(k_L^2 + 3\Omega) - (k_L^2 - 5\Omega)c_0\big]q_x^2 + 4c_2^3 q_x^2 + \tfrac{1}{2}\big[2k_L^4 + 9\Omega^2 + (k_L^2 + 6\Omega)c_0\big]q_x^4 \\
& + \tfrac{1}{2}(3\Omega + c_0)q_x^6 + \tfrac{3}{16}q_x^8 + 4c_2^2\big[\Omega^2 + (k_L^2 - \Omega + c_0)q_x^2\big] \\
& - \tfrac{1}{2}c_2\big[16\Omega^3 + 2\Omega(7k_L^2 + 5\Omega + 8c_0)q_x^2 + (k_L^2 + 6\Omega + 4c_0)q_x^4 + q_x^6\big],
\end{aligned} \tag{A8}$$

$$\begin{aligned}
d = {} & -\tfrac{1}{64}q_x^2\big[\big(4k_L^2 - 4\Omega - q_x^2\big)(2\Omega + q_x^2) + c_2\big(-8k_L^2 + 8\Omega + 4q_x^2\big)\big]\big\{-4c_0\big[8\Omega^2 - 2(k_L^2 - 3\Omega)q_x^2 \\
& + q_x^4 - 4c_2(2\Omega + q_x^2)\big] + (2\Omega + q_x^2)\big[-16\Omega c_2 + 16c_2^2 - q_x^2\big(-4k_L^2 + 4\Omega + q_x^2\big)\big]\big\}.
\end{aligned} \tag{A9}$$

[1] Y.-J. Lin, K. Jiménez-García, and I. B. Spielman, Spin–orbit-coupled Bose–Einstein condensates, Nature (London) **471**, 83 (2011).

[2] D. Campbell, R. Price, A. Putra, A. Valdés-Curiel, D. Trypogeorgos, and I. Spielman, Magnetic phases of spin-1 spin–orbit-coupled Bose gases, Nat. Commun. **7**, 10897 (2016).

[3] X. Luo, L. Wu, J. Chen, Q. Guan, K. Gao, Z.-F. Xu, L. You, and R. Wang, Tunable atomic spin-orbit coupling synthesized with a modulating gradient magnetic field, Sci. Rep. **6**, 18983 (2016).

[4] Q. Zhu, C. Zhang, and B. Wu, Exotic superfluidity in spin-orbit coupled Bose-Einstein condensates, Europhys. Lett. **100**, 50003 (2012).

[5] J.-R. Li, J. Lee, W. Huang, S. Burchesky, B. Shteynas, F. Ç. Top, A. O. Jamison, and W. Ketterle, A stripe phase with supersolid properties in spin–orbit-coupled Bose–Einstein condensates, Nature (London) **543**, 91 (2017).

[6] W.-L. Xia, L. Chen, T.-T. Li, Y. Zhang, and Q. Zhu, Metastable supersolid in spin-orbit-coupled Bose-Einstein condensates, Phys. Rev. A **107**, 053302 (2023).

[7] I. A. Bhat, T. Mithun, B. A. Malomed, and K. Porsezian, Modulational instability in binary spin-orbit-coupled Bose-Einstein condensates, Phys. Rev. A **92**, 063606 (2015).

[8] S. Bhuvaneswari, K. Nithyanandan, P. Muruganandam, and K. Porsezian, Modulation instability in quasi-two-dimensional spin–orbit coupled Bose–Einstein condensates, J. Phys. B **49**, 245301 (2016).

[9] G.-Q. Li, G.-D. Chen, P. Peng, Z. Li, and X.-D. Bai, Modulation instability of a spin-1 Bose–Einstein condensate with spin–orbit coupling, J. Phys. B **50**, 235302 (2017).

[10] J. Radić, T. A. Sedrakyan, I. B. Spielman, and V. Galitski, Vortices in spin-orbit-coupled Bose-Einstein condensates, Phys. Rev. A **84**, 063604 (2011).

[11] S. Adhikari, Vortex-lattice formation in a spin–orbit coupled rotating spin-1 condensate, J. Phys.: Condens. Matter **33**, 065404 (2021).

[12] V. Achilleos, D. J. Frantzeskakis, P. G. Kevrekidis, and D. E. Pelinovsky, Matter-wave bright solitons in spin-orbit coupled Bose-Einstein condensates, Phys. Rev. Lett. **110**, 264101 (2013).

[13] Y. Xu, Y. Zhang, and B. Wu, Bright solitons in spin-orbit-coupled Bose-Einstein condensates, Phys. Rev. A **87**, 013614 (2013).

[14] T. Ohmi and K. Machida, Bose-Einstein condensation with internal degrees of freedom in alkali atom gases, J. Phys. Soc. Jpn. **67**, 1822 (1998).

[15] T.-L. Ho, Spinor Bose condensates in optical traps, Phys. Rev. Lett. **81**, 742 (1998).

[16] H. Wang, A time-splitting spectral method for computing dynamics of spinor F=1 Bose–Einstein condensates, Comput. Math. **84**, 925 (2007).

[17] W. Bao and F. Y. Lim, Computing ground states of spin-1 Bose–Einstein condensates by the normalized gradient flow, SIAM J. Sci. Comput. **30**, 1925 (2008).

[18] F. Y. Lim and W. Bao, Numerical methods for computing the ground state of spin-1 Bose-Einstein condensates in a uniform magnetic field, Phys. Rev. E **78**, 066704 (2008).

[19] P. Muruganandam and S. K. Adhikari, Fortran programs for the time-dependent Gross–Pitaevskii equation in a fully anisotropic trap, Comput. Phys. Commun. **180**, 1888 (2009).

[20] R. Ravisankar, D. Vudragović, P. Muruganandam, A. Balaž, and S. K. Adhikari, Spin-1 spin–orbit-and Rabi-coupled Bose–Einstein condensate solver, Comput. Phys. Commun. **259**, 107657 (2021).

[21] Y.-K. Liu and S.-J. Yang, Exact solitons and manifold mixing dynamics in the spin-orbit–coupled spinor condensates, Europhys. Lett. **108**, 30004 (2014).

[22] S. K. Adhikari, Multiring, stripe, and superlattice solitons in a spin-orbit-coupled spin-1 condensate, Phys. Rev. A **103**, L011301 (2021).

[23] S. K. Adhikari, Symbiotic solitons in quasi-one- and quasi-two-dimensional spin-1 condensates, Phys. Rev. E **104**, 024207 (2021).

[24] S. K. Adhikari, Stable multi-peak vector solitons in spin–orbit coupled spin-1 polar condensates, Physica E **118**, 113892 (2020).

[25] J. He and J. Lin, Stationary and moving bright solitons in Bose–Einstein condensates with spin–orbit coupling in a Zeeman field, New J. Phys. **25**, 093041 (2023).

[26] S. Mardonov, M. Modugno, and E. Y. Sherman, Dynamics of spin-orbit coupled Bose-Einstein condensates in a random potential, Phys. Rev. Lett. **115**, 180402 (2015).

[27] S. Mardonov, V. V. Konotop, B. A. Malomed, M. Modugno, and E. Y. Sherman, Spin-orbit-coupled soliton in a random potential, Phys. Rev. A **98**, 023604 (2018).

[28] S. Mardonov, M. Modugno, E. Y. Sherman, and B. A. Malomed, Rabi-coupling-driven motion of a soliton in a Bose-Einstein condensate, Phys. Rev. A **99**, 013611 (2019).

[29] N. Bogoliubov, On the theory of superfluidity, J. Phys. (U.S.S.R.) **11**, 23 (1947).

[30] A. L. Fetter, Ground state and excited states of a confined condensed Bose gas, Phys. Rev. A **53**, 4245 (1996).

[31] M. Edwards, P. A. Ruprecht, K. Burnett, R. J. Dodd, and C. W. Clark, Collective excitations of atomic Bose-Einstein condensates, Phys. Rev. Lett. **77**, 1671 (1996).

[32] K. G. Singh and D. S. Rokhsar, Collective excitations of a confined Bose condensate, Phys. Rev. Lett. **77**, 1667 (1996).

[33] S. Stringari, Collective excitations of a trapped Bose-condensed gas, Phys. Rev. Lett. **77**, 2360 (1996).

[34] E. V. Goldstein and P. Meystre, Quasiparticle instabilities in multicomponent atomic condensates, Phys. Rev. A **55**, 2935 (1997).

[35] T. Ozawa, L. P. Pitaevskii, and S. Stringari, Supercurrent and dynamical instability of spin-orbit-coupled ultracold Bose gases, Phys. Rev. A **87**, 063610 (2013).

[36] D. S. Jin, J. R. Ensher, M. R. Matthews, C. E. Wieman, and E. A. Cornell, Collective excitations of a Bose-Einstein condensate in a dilute gas, Phys. Rev. Lett. **77**, 420 (1996).

[37] M.-O. Mewes, M. R. Andrews, N. J. van Druten, D. M. Kurn, D. S. Durfee, C. G. Townsend, and W. Ketterle, Collective excitations of a Bose-Einstein condensate in a magnetic trap, Phys. Rev. Lett. **77**, 988 (1996).

[38] M. A. Khamehchi, Y. Zhang, C. Hamner, T. Busch, and P. Engels, Measurement of collective excitations in a spin-orbit-coupled Bose-Einstein condensate, Phys. Rev. A **90**, 063624 (2014).

[39] R. Ravisankar, H. Fabrelli, A. Gammal, P. Muruganandam, and P. K. Mishra, Effect of Rashba spin-orbit and Rabi couplings on the excitation spectrum of binary Bose-Einstein condensates, Phys. Rev. A **104**, 053315 (2021).

[40] K. Kasamatsu and M. Tsubota, Multiple domain formation induced by modulation instability in two-component Bose-Einstein condensates, Phys. Rev. Lett. **93**, 100402 (2004).

[41] K. Kasamatsu and M. Tsubota, Modulation instability and solitary-wave formation in two-component Bose-Einstein condensates, Phys. Rev. A **74**, 013617 (2006).

[42] N. P. Robins, W. Zhang, E. A. Ostrovskaya, and Y. S. Kivshar, Modulational instability of spinor condensates, Phys. Rev. A **64**, 021601(R) (2001).

[43] W. Zhang, D. L. Zhou, M.-S. Chang, M. S. Chapman, and L. You, Dynamical instability and domain formation in a spin-1 Bose-Einstein condensate, Phys. Rev. Lett. **95**, 180403 (2005).

[44] M. Matuszewski, T. J. Alexander, and Y. S. Kivshar, Spin-domain formation in antiferromagnetic condensates, Phys. Rev. A **78**, 023632 (2008).

[45] M. Matuszewski, Rotonlike instability and pattern formation in spinor Bose-Einstein condensates, Phys. Rev. Lett. **105**, 020405 (2010).

[46] J. Kronjäger, C. Becker, P. Soltan-Panahi, K. Bongs, and K. Sengstock, Spontaneous pattern formation in an antiferromagnetic quantum gas, Phys. Rev. Lett. **105**, 090402 (2010).

[47] Z. Pu, J. Zhang, S. Yi, D. Wang, and W. Zhang, Magnetic-field-induced dynamical instabilities in an antiferromagnetic spin-1 Bose-Einstein condensate, Phys. Rev. A **93**, 053628 (2016).

[48] S. K. Gangwar, R. Ravisankar, H. Fabrelli, P. Muruganandam, and P. K. Mishra, Emergence of unstable avoided crossing in the collective excitations of spin-1 spin-orbit-coupled Bose-Einstein condensates, Phys. Rev. A **109**, 043306 (2024).

[49] N. R. Bernier, E. G. Dalla Torre, and E. Demler, Unstable avoided crossing in coupled spinor condensates, Phys. Rev. Lett. **113**, 065303 (2014).

[50] L. Salasnich, A. Parola, and L. Reatto, Effective wave equations for the dynamics of cigar-shaped and disk-shaped Bose condensates, Phys. Rev. A **65**, 043614 (2002).

[51] S. Gautam and S. K. Adhikari, Mobile vector soliton in a spin–orbit coupled spin-1 condensate, Laser Phys. Lett. **12**, 045501 (2015).

[52] G. Katsimiga, S. Mistakidis, P. Schmelcher, and P. Kevrekidis, Phase diagram, stability and magnetic properties of nonlinear excitations in spinor Bose–Einstein condensates, New J. Phys. **23**, 013015 (2021).

[53] Y. Kawaguchi and M. Ueda, Spinor Bose–Einstein condensates, Phys. Rep. **520**, 253 (2012).

[54] D. M. Stamper-Kurn and M. Ueda, Spinor Bose gases: Symmetries, magnetism, and quantum dynamics, Rev. Mod. Phys. **85**, 1191 (2013).

[55] S. Inouye, M. Andrews, J. Stenger, H.-J. Miesner, D. M. Stamper-Kurn, and W. Ketterle, Observation of Feshbach resonances in a Bose–Einstein condensate, Nature (London) **392**, 151 (1998).

[56] A. Marte, T. Volz, J. Schuster, S. Dürr, G. Rempe, E. G. M. van Kempen, and B. J. Verhaar, Feshbach resonances in rubidium 87: Precision measurement and analysis, Phys. Rev. Lett. **89**, 283202 (2002).

[57] C. Chin, R. Grimm, P. Julienne, and E. Tiesinga, Feshbach resonances in ultracold gases, Rev. Mod. Phys. **82**, 1225 (2010).

[58] Q.-L. Zhu, L. Pan, and J. An, Spin-orbit-coupled spin-1 Bose-Einstein-condensate flow past an obstacle in the presence of a Zeeman field, Phys. Rev. A **102**, 053320 (2020).

[59] E. Anderson, Z. Bai, C. Bischof, L. S. Blackford, J. Demmel, J. Dongarra, J. Du Croz, A. Greenbaum, S. Hammarling, A. McKenney, and D. Sorensen, *LAPACK Users' Guide* (SIAM, Philadelphia, 1999).

[60] M. Abad and A. Recati, A study of coherently coupled two-component Bose-Einstein condensates, Eur. Phys. J. D **67**, 148 (2013).

[61] R. Ravisankar, T. Sriraman, L. Salasnich, and P. Muruganandam, Quenching dynamics of the bright solitons and other localized states in spin–orbit coupled Bose–Einstein condensates, J. Phys. B **53**, 195301 (2020).

[62] G. I. Martone, Y. Li, L. P. Pitaevskii, and S. Stringari, Anisotropic dynamics of a spin-orbit-coupled Bose-Einstein condensate, Phys. Rev. A **86**, 063621 (2012).

[63] Z.-Q. Yu, Phase transitions and elementary excitations in spin-1 Bose gases with Raman-induced spin-orbit coupling, Phys. Rev. A **93**, 033648 (2016).

[64] T. Mithun and K. Kasamatsu, Modulation instability associated nonlinear dynamics of spin–orbit coupled Bose–Einstein condensates, J. Phys. B **52**, 045301 (2019).

[65] R. S. Tasgal and Y. B. Band, Sound waves and modulational instabilities on continuous-wave solutions in spinor Bose-Einstein condensates, Phys. Rev. A **91**, 013615 (2015).

[66] A. Putra, F. Salces-Cárcoba, Y. Yue, S. Sugawa, and I. B. Spielman, Spatial coherence of spin-orbit-coupled Bose gases, Phys. Rev. Lett. **124**, 053605 (2020).

[67] Ritu, Rajat, A. Roy, and S. Gautam, Thermal amplification and melting of phases in spin–orbit-coupled spin-1 Bose–Einstein condensates, New J. Phys. **27**, 043005 (2025).

[68] https://iitgoffice-my.sharepoint.com/:u:/g/personal/pankaj_mishra_iitg_ac_in/Eb8aGAuydHZOh06VZRV6u4oBdJg7NGU8grfOksl5zROhSw?e=kZ1oD1.